Optimizing Silicon Chip Thickness and Pixel Activation Threshold in Scanning Transmission Electron Microscope Detectors

CNF Summer Student: Himani Anilkumar Mishra Student Affiliation: School of Applied and Engineering Physics, Cornell University

Summer Program(s): 2025 Cornell NanoScale Facility Research Experience for Undergraduates (CNF REU) Program, SUPREME REU

Principal Investigator(s): David A. Muller, School of Applied and Engineering Physics, Cornell University

Mentor(s): Steven E. Zeltmann, Platform for the Accelerated Realization, Analysis, and Discovery of Interface Materials (PARADIM), Cornell University

Primary Source(s) of Research Funding: National Science Foundation under Grant No. NNCI-2025233, SUPREME

Contact: ham74@cornell.edu, steven.zeltmann@cornell.edu, david.a.muller@cornell.edu

Summer Program Website(s): https://cnf.cornell.edu/education/reu

Research Group Website: https://muller.research.engineering.cornell.edu/

Abstract:

Electron ptychography is a scanning transmission electron microscopy (STEM) technique used to achieve high-quality three-dimensional characterization of rapidly shrinking semiconductor devices1. We aim to design dose-efficient STEM detectors that use the maximal amount of generated signal. In STEM, a focused beam of electrons are either transmitted and/ or scattered by our material of interest. The transmitted electrons then encounter a pixel array detector that is composed of a sensor layer, which is bump-bonded to an ASIC^{2,3}. The silicon sensor layer is divided into pixels that record the amount of energy deposited by the electrons. Each pixel has a threshold of activation. If an electron deposits energy greater than the threshold, the pixel is activated. The problem lies in when the electron lands on the intersection of pixels. If the threshold is low, all pixels are triggered, leading to overcounting, but if the threshold is high, no pixels are triggered, leading to undercounting. Therefore, we must find the optimal pixel activation threshold value. We also test different thicknesses for the sensor layer to avoid the problem of oversaturation. We use a Monte Carlo simulation to track the trajectories and energies deposited by an incident beam of electrons in the sensor layer. From this, we analyze energy distributions and calculate the modulation transfer function (MTF) and detective quantum efficiency (DQE)^{4,6} to evaluate the performance of different thickness levels and pixel activation thresholds. Careful thresholding in conjunction with thickness optimization will enable dose-efficient STEM for the high-quality characterization of next-generation semiconductors.

Summary of Research:

The pixel array detector is a type of electron microscope detector that offers high-speed data collection due to its parallel pixel readout and sensitivity to signal changes. It is composed of two layers: a sensor layer and CMOS Integrated Chip. The sensor layer is sectioned into square pixels. This layer is then bump-bonded to the

IC. When the energy deposited in a given pixel by an electron is greater than the pixel activation threshold value, the pixel is activated. The problem lies in when an electron lands on the intersection of pixels. A low pixel activation threshold will lead to the electron depositing enough energy in all the pixels and activating all of them, resulting in overcounting. A high threshold will lead to the electron not depositing enough energy in any of the pixels and activating none of them, resulting in undercounting.

To study the relationships between sensor layer thickness and pixel activation threshold on the modulation transfer function (MTF) and detective quantum efficiency (DQE) of our system, we modeled the spread of electrons using a Monte Carlo simulation in a 500-micron deep silicon layer. We set varying initial beam voltages, from 60keV to 300keV. We created lateral and depth energy spread distributions, tracking electron energy at each location.

Summing over the Y and Z direction (Z direction is the beam direction, X-Y is the lateral plane) of the silicon, we created a line spread function, plotting the energy as a function of X position. Taking the Fourier transform of the LSF produces the MTF3. Then, we analyze the relationship between different silicon thickness and activation thresholds, performing the simulation for different pairs and plotting the MTF at Nyquist frequency (contrast for the smallest features) and DQE at 0 frequency (noise for the largest features).

We are also interested in studying the behavior of the Timepix4, a thinner detector, with a 300µm-deep Si layer. Using this depth and a 150 keV threshold, we analyze the relationship between beam radius and pixel size. We choose this threshold because it produces a good MTF. A 150 keV threshold corresponds to around 72.7% of the total energy deposition. This energy is contained in a radius of around 244µm, or 4.5 pixels. We map counts for each triggered pixel.

The origin receives the most energy, resulting in the greatest counts. Fewer pixels are triggered near the edge. At a low threshold, a higher ratio of beam radius to pixel width is favored and at high threshold, a lower

ratio of beam radius to pixel width is favored. I also create a pixel activation map for a 300-micron-deep silicon layer (depth of the Timepix4 sensor layer)5, and 150keV threshold and look at the relationship between the initial beam spread and the pixel width.

Conclusions and Future Steps:

Higher initial beam voltages have LSF's with broad tails, as the electrons spread further, both laterally and in depth. Smaller initial beam voltages have sharper LSF's, as the electrons don't have as much lateral or depth spread. Lower beam energies are closer to the ideal MTF because they trigger fewer pixels, producing greater contrast. Lower sensor layer thickness and higher threshold (up to an optimal point) favor higher MTF for the same reason.

Lower thicknesses obtain a better MTF for low thickness, because the electrons' spread is limited, resulting in a smaller radius of energy deposition. Each electron activates only a few pixels, resulting in better contrast. The optimal threshold for a good MTF appears to be around 125 keV for 100, 200, 400 and 500- μ m depth, after which point the MTF decreases for higher thresholds. 300- μ m depth seems to have the optimal MTF around 150keV. Thus, there is an optimal point for the threshold, around 100-150keV, for most thicknesses between 100 to 500 μ m.

Meanwhile, DQE is favored by higher sensor layer thickness, because a greater depth allows us to capture the entire spread of the electron, resulting in greater signal acquisition. A higher DQE is also favored by a lower pixel activation threshold because it allows each electron to consistently activate many pixels, producing less noise. At a low threshold, a higher ratio of beam radius to pixel width is favored and at high threshold, a lower ratio of beam radius to pixel width is favored. Thus, MTF and DQE are favored by opposite trends in thickness and threshold. It is important to assess these metrics for each distinct detector design to find the optimal conditions for both metrics. In the future, we will perform the Monte Carlo simulation with more electrons (at least 100,000) for a more detailed understanding of the relationship between thickness and threshold.

We may also consider how detectors with fewer pixels can attain maximal signal capture, as MTF and DQE may be easier to optimize for fewer pixels. Additionally, we can quantify the maximal usable imaging speed (MUIS), in addition to MTF and DQE, to assess different detector designs.

Acknowledgements:

Thank you to my mentor, Steven E. Zeltmann, and Principal Investigator, Professor David Muller for their support and guidance on this project. Thank you to the NSF/SRC SUPREME REU Program and the Cornell Nanoscale Facility (NNCI-2025233) for funding and supporting this project.

References:

- S. Karapetyan, S. Zeltmann, T.-K. Chen, V. D. H. Hou, and D. A. Muller, Visualizing Defects and Amorphous Materials in 3D with Mixed-State Multislice Electron Ptychography, Microscopy and Microanalysis 30, (2024).
- [2] H. T. Philipp et al., Very-High Dynamic Range, 10,000 Frames/ Second Pixel Array Detector for Electron Microscopy, Microsc

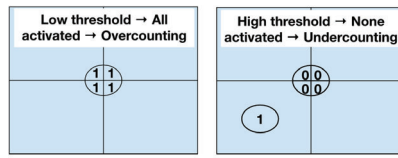


Figure 1: When an electron lands on intersection of pixels, there may be overcounting if the pixel activation threshold is too low and undercounting if the threshold is too high.

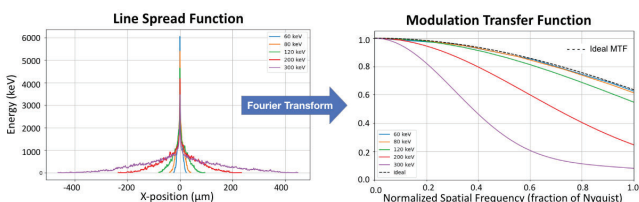


Figure 2: This line spread function (LSF) sums all the energy deposited from 1000 electrons in the Y and Z directions and plots the energy distribution as a function of X position. The Fourier transform of the LSF is the MTF.

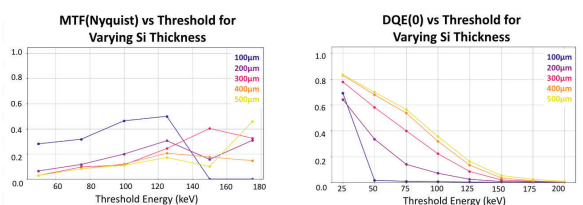


Figure 3: MTF at Nyquist frequency and DQE at zero frequency for varying silicon thicknesses and pixel activation thresholds.

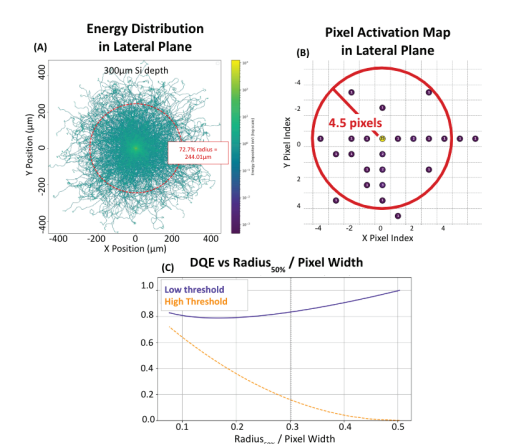


Figure 4: (A) Radius of energy distribution that corresponds to a 150keV threshold. (B) Pixel activation map for 300-µm thick silicon layer. (C) Relationship between ratio of radius where 50% of energy is distributed to pixel width and DQE.

Microanal 28, 425 (2022).

- [3] M. W. Tate et al., High Dynamic Range Pixel Array Detector for Scanning Transmission Electron Microscopy, Microsc Microanal 22, 237 (2016).
- [4] G. McMullan, S. Chen, R. Henderson, and A. R. Faruqi, Detective quantum efficiency of electron area detectors in electron microscopy, Ultramicroscopy 109, 1126 (2009).
- [5] N. Dimova et al., Measurement of the Resolution of the Timepix4 Detector for 100 keV and 200 keV Electrons for Transmission Electron Microscopy, Nuclear Instruments and Methods in Physics Research Section A: Accelerators, Spectrometers, Detectors and Associated Equipment 1075, 170335 (2025).
- [6] A. Gnanasambandam and S. H. Chan, Exposure-Referred Signal-to-Noise Ratio for Digital Image Sensors, arXiv:2112.05817.

Initiated CVD (iCVD) Polymerization in Liquid Crystal to Synthesize Polymer Particles

CNF Summer Student: Eva Reed Student Affiliation: Chemical Engineering, Princeton University

Summer Program(s): 2025 Cornell NanoScale Facility Research Experience for Undergraduates (CNF REU) Program,

SUPREME REU

Principal Investigator(s): Nicholas Abbott, Rong Yang

Mentor(s): Shiqi Li

Primary Source(s) of Research Funding: Future Manufacturing award to Cornell Chemical Engineering, FMRG: Cyber: Scalable Precision Manufacturing of Programmable Polymer Nanoparticles Using Low-temperature Initiated Chemical Vapor Deposition Guided by Artificial Intelligence, funded by the National Science Foundation under award CMMI-2229092

Contact: ryang@cornell.edu, nla34@cornell.edu, er564@cornell.edu, sl2869@cornell.edu

Summer Program Website(s): https://cnf.cornell.edu/education/reu

Research Group Website: https://theyanglab.com/

Primary CNF Tools Used: Leica 300 CPD, Zeiss Supra SEM

Abstract:

Synthesis schemes targeting specific nanoscale polymer architectures have the potential to advance the efficacy of polymer materials for applications in biomaterials and beyond as tunable material solutions [1]. In our current work, we expand previous investigations of the synthesis pathway of divinylbenzene (DVB) via initiated chemical vapor deposition (iCVD) templated in nematic liquid crystals to begin to explore polymerization with alternative monomers and process conditions. Understanding the effect of tuning the precursor concentrations and substrate properties on the resultant polymer architectures will empower future efforts to produce shape-controlled polymer particles within this synthesis pathway.

Summary of the Research:

Many existing methods to control polymer microparticle architectures involve physical manipulations, which are difficult to scale [1]. Initiated chemical vapor deposition (iCVD) within a liquid crystal (LC) template provides a pathway to construct polymer nanoscale and microparticles with specific architectures achievable based on the reaction conditions [2]. In iCVD, the polymer precursors-the monomer and initiator-are delivered continuously in vapor phase into a chamber alongside an inert carrier gas. A superheated filament radicalizes the initiator to allow the polymerization reaction to proceed. As the monomer and initiator molecules adsorb onto the substrate, free-radical polymerization occurs. iCVD eliminates the need for solvent-mediated reactions, which can result in impure polymer products, impacting the functionality and applicability of functionalized polymeric materials [3].

The innovation that inspired this project is the use of a liquid crystal (E7, a commodity liquid crystal containing a eutectic mixture of cyanobiphenyls

and terphenyls) as a templating material rather than an isotropic (disordered) liquid. Liquid crystals are a phase of matter in between liquid and crystalline solids that acquire exciting and useful properties from heightened orientational and positional ordering of their constituent molecular subunits [5]. Researchers have taken advantage of the molecular level organization in these materials in iCVD systems to guide the polymerization process and control the particles' final conformation [2]. The identity of the substrate on which the film is prepared controls the properties and orientation of the mesogens within the LC thin-film. At the LC-air interface E7 adopts a perpendicular anchoring scheme while at the interface with untreated glass the mesogens will be anchored planarly in multidomains. Chemical treatments octadecyltrichlorosilane Dimethyloctadecyl(3-(trimethoxysilyl) and propyl)ammonium chloride (DMOAP) result in planar anchoring at the LC-substrate surface as well as inducing a single homeotropic domain across the LC film [1]. Representative illustrations of the different anchoring conditions are included in Figure 1. These treatment schemes offer the researcher an additional layer of control to the polymer template during the reaction. In addition to comparing polymer products on substrates with homolayers of OTS, and DMOAP treatments, gradient substrates prepared by the Genzer group at NC State-gradients of OTS to glass, DMOAP to glass,

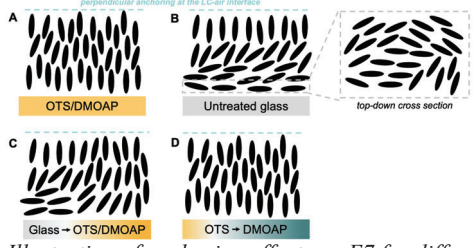


Figure 1: Illustration of anchoring effects on E7 for different substrate types.

and OTS to DMOAP counter gradients—were reacted to provide a comparison of both anchoring condition and the impact of anchoring strength and surface energy [5].

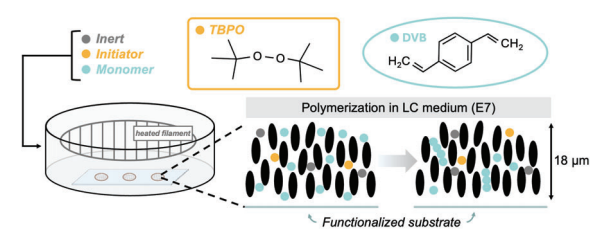


Figure 2: Schematic of in-lab set up for iCVD. Adapted from [1]: Jain, A. Science Advances 2024, 10 (45). https://doiorg/10.1126sciadv.adp5573.

Our experimental system, illustrated in Figure 2, reacts with controlled amounts of vaporized monomer and initiator tert-butyl peroxide (TBPO). The reaction takes place in a TEM grid containing nematic phase liquid crystal films (E7, TNI=60-63°C) mounted on a range of untreated and treated substrates. The chamber pressure is regulated to 150 mTorr and the sample stage is maintained at 20 °C. The reaction process is monitored in situ by a long focal length set up of a Keyence VHX 970F microscope and after reaction progress has been halted by SEM, confocal imaging, and microscopy on an Olympus BX41 microscope equipped with 4× and 20× objectives. Reactions were carried out at both high initiator to monomer ratios (~0.7 Monomer/Initiator) and low ratios (~ 0.15) at times ranging from 75 to 140 minutes. Critical point drying was employed to remove liquid crystal films while preserving the particles formed for imaging by SEM [1].

Conclusion and Future Steps:

Optical micrographs of films prepared on glass and homolayers of OTS and DMOAP showed that arrays of polymer nanospheres formed with greater regularity and covered a higher percentage of the available film area on DMOAP and glass than the OTS substrate (Figure 3). Analysis of particle sizes showed little significant variation in particle diameter between homolayer substrates: an observation confirmed with SEM imaging of representative polymer particles and particle clusters (Figure 4). Reactions performed on gradient films mirror this trend, with the sections of the film treated with DMOAP displaying a greater proportion of particle arrays than OTS. Analysis of reactions on the OTS to DMOAP gradient film further confirmed this trend, indicating that the anchoring orientation did not impact the formation of particle arrays. An implication of this finding is that the polymerization process occurs in the bulk LC or at the LC-air interface rather than on the LCsubstrate interface. This hypothesis was supported by confocal microscopy which revealed that the nanosphere particles were positioned along a single focal plane within the LC bulk.

Determining the location of particle formation during the initiation and growth processes deepens knowledge of the dynamics of the polymerization reaction and,

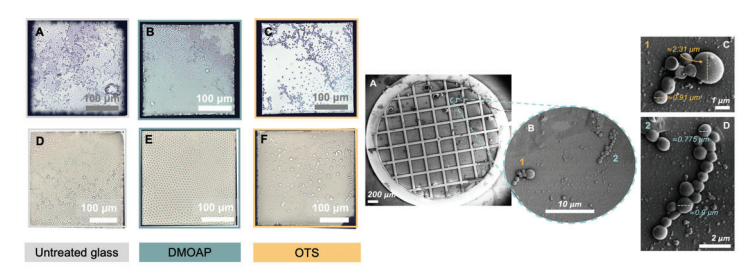


Figure 3 (Left): White balanced optical micrographs showing the polymer products formed from high initiator to monomer ratio conditions (17.1 mTorr P(TBPO)/25.1 mTorr P(DVB)) (A-C) and low initiator to monomer ratio conditions (10.6 mTorr P(TBPO)/69 mTorr P(DVB)) (D-F). The DMOAP treated films (B,E) create more regular particle arrays than the untreated glass films (A,D) or the OTS treated films (C,F).

Figure 4 (Right): SEM images showing polymer nanoparticles. Low magnification (A) and high magnification are shown (B) alongside measurements of the range of particle diameters are also displayed (C, D).

in turn, will offer researchers greater insight into controlling the polymer architectures formed within the LC films. Future work will bring in more advanced imaging and characterization techniques, including AFM and advanced confocal microscopy, to detail this polymerization process and allow our understanding to empower iCVD studies of other monomer systems.

Acknowledgements:

This work was performed in part at the Cornell NanoScale Facility, a member of the National Nanotechnology Coordinated Infrastructure (NNCI), which is supported by the National Science Foundation (Grant NNCI-2025233). This work is further funded by a Future Manufacturing award to Cornell Chemical Engineering, FMRG: Cyber: Scalable Precision Manufacturing of Programmable Polymer Nanoparticles Using Low-temperature Initiated Chemical Vapor Deposition Guided by Artificial Intelligence, funded by the National Science Foundation under award CMMI-2229092 and finally the NIH S10RR025502 grant to the BRC for the Zeiss LSM 710 confocal microscope.

- Jain, A et al., Single-step synthesis of shaped polymeric particles using initiated chemical vapor deposition in liquid crystals. Sci. Adv. 2024 10, eadp5573. DOI:10.1126/sciadv. adp5573..
- [2] Cheng, Z.; Lee, H.; Kim, T.; et al. Templated Nanofiber Synthesis via Chemical Vapor Polymerization into Liquid Crystalline Films. Science 2018, 360 (6391), 804–808. https://doi.org/10.1126/science.aar8449
- [3] Bradley, L. C.; Gupta, M. Microstructured Films Formed on Liquid Substrates via Initiated Chemical Vapor Deposition of Cross-Linked Polymers. Langmuir 2015, 31 (29), 7999–8005. https://doi.org/10.1021/acs.langmuir.5b01663.
- [4] De Luna, M. S.; Torres, C. A.; Chen, H.; et al. Interactions between Polymers and Liquids during Initiated Chemical Vapor Deposition onto Liquid Substrates. Mol. Syst. Des. Eng. 2020, 5 (1), 15–21. https://doi.org/10.1039/c9me00087a.
- [5] Clare, B. H.; Efimenko, K.; Fischer, D. A.; Genzer, J.; Abbott, N. L. Orientations of Liquid Crystals in Contact with Surfaces That Present Continuous Gradients of Chemical Functionality. Chem. Mater. 2006, 18 (9), 2357–2363. https://doi.org/10.1021/cm052537n.

Computer Vision Applied to Polymer Particles in Liquid Crystal (LC) to Enable On-the-Fly Characterization of their Morphology and Size Distribution, Among Other Properties

CNF Summer Student: William Sober Student Affiliation: Physics, Amherst College

Summer Program(s): 2025 Cornell NanoScale Facility Research Experience for Undergraduates (CNF REU) Program,

SUPREME REU

Principal Investigator(s): Nicholas Abbott, Fengqi You

Mentor(s): Soumyamouli Pal

Primary Source(s) of Research Funding: National Science Foundation award NNCI- 2025233, Center for Energy Efficient Magnonics (DE-AC02- 76SF00515), Department of Energy Office of Science, Basic Energy Sciences (DE-SC0019997)

Contact: nla 34 @cornell.edu, fengqi.you @cornell.edu, will sober @gmail.com

Summer Program Website(s): https://cnf.cornell.edu/education/reu

Abstract:

Monitoring polymerization reactions in-situ provides many advantages like real-time feedback for tuning conditions and viewing undisturbed growth. However, image quality can be reduced due to difficulties in viewing the reaction such as vibrations and long working distances with a microscope. This project explores approaches to enhance lower quality in-situ microscope images of polymers in liquid crystal from an initiated chemical vapor deposition (iCVD) reactor by using an enhanced super resolution generative adversarial network (ESRGAN). To train ESRGAN, polymer test systems were set up in an iCVD reactor, and low-quality in-situ images of the polymers were taken along with corresponding high-quality exsitu images. We cropped matching single-cluster images and applied different pre-processing techniques while varying hyperparameters such as learning rate and weight decay. The accuracy of these methods was evaluated with the Structural Similarity Index Measure (SSIM) and visually compared to the reference high-quality images. We found that overall, ESRGAN has strong potential for polymer image enhancement, and changeable hyperparameters gives it versatility for different images. However, further model optimization is needed before it is adapted for real polymerization images. The adaptability of ESRGAN makes this approach applicable for more varied use like new types of polymers or different microscope setups.

Summary of Research:

Initiated chemical vapor deposition (iCVD) in liquid crystal (LC) has the capability to produce

tunable polymer growths like nanospheres with potential for use in drug delivery or separations for chromatography1. Insitu monitoring of the reaction is possible through a window with a long-distance focal length lens Keyence VHX 970F microscope. However, issues with vibrations and external noise are compounded by the viewing distance, so the images from the microscope are blurry and low-quality. The samples can be high-quality ex-situ imaged by an Olympus BX41 microscope although this requires stopping the reaction to remove samples, which can also disturb polymers.

With the assistance of a machine learning-based approach, we can enhance the in-situ images to more closely match the quality of the high-quality ex-situ images. Previous preliminary research has found that the enhanced superresolution generative adversarial networks (ESRGAN) model outperforms other models for this purpose.

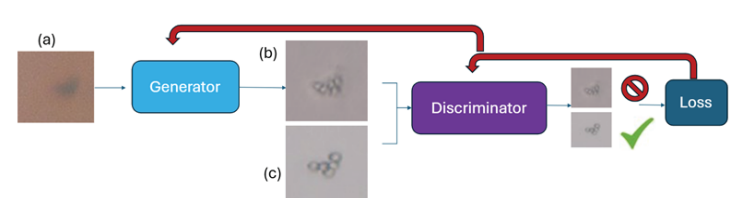


Figure 1: Diagram of ESRGAN structure. The generator takes low-quality images (a) and enhances them (b). The discriminator detects real (c) from fake images and then model updates from loss functions.

ESRGAN has two key components: the generator and the discriminator (Figure 1). For training, the generator takes a low-quality image and tries to enhance it to look like a high-quality image. The discriminator is then given that enhanced image along with the actual high-quality image and tries to determine which is the real one. Then the model calculates loss functions for how poorly the generator and discriminator performed so that the generator and discriminator can improve their weights. This process is iterative, with the generator and discriminator improving each other thousands of steps. In

addition to the images used for training, many are set aside solely for testing the performance of the model to limit overfitting.

We tried multiple configurations of ESRGAN by varying hyperparameters, which are parameters in ESRGAN that can be adjusted to change how the model learns. We mainly looked at learning rate (.0001-.001), weight decay (0 or .0001), and number of epochs(10-300).

A test system was created using commercially available 5μ polystyrene spheres dispersed in the liquid crystal, allowing for fixed particle sizes and faster data collection compared to growing polymers.

Training the model with images of the entire LC grid causes complications with identifying the same polymer across low and high-quality images, therefore we used 64x64 pixel cropped patches, 32x32 pixel downscaled cropped patches, and 64x64 images where the contour of the particle was cropped and the background was replaced with white (Figure 2).

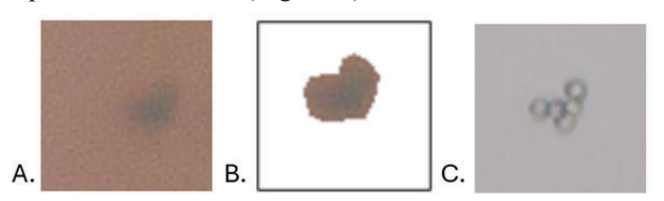


Figure 2: A. Low quality cropped polymer cluster, with B. its contour cropped and C. their high-quality reference. These images were used as three different training inputs for ESRGAN.

Conclusions and Future Steps:

As an exploratory project, a main goal of this project was to explore the feasibility of different approaches. Weight decay stabilized training of the 64x64 images and produced best overall results. Conversely, with 32x32 images, removing weight decay allowed the model to make riskier, but successful, improvements. While contour cropping the particles was not effective, ESRGAN was generally robust against noise. The main limitation was particle size estimation accuracy (Figure 3), likely due to inconsistent scaling during

preprocessing. Remaking the dataset may resolve this issue. Overall, these findings establish a strong foundation for adapting ESRGAN for polymerization imaging.

For future development, ESRGAN should be adapted to work on real polymerization images, and polymers of different sizes. Training on lower magnification images would be more effective at capturing more polymers in the frame, fitting six full grids into the frame instead of one. Implementing the model with video capabilities would aid in faster and more convenient analysis during reactions. Applying a different de-noising program to the low and high quality images could also potentially increase the ground truth image quality and accelerate training.

References:

[1] Apoorva Jain et al., Single-step synthesis of shaped polymeric particles using initiated chemical vapor deposition in liquid crystals. Sci. Adv. 10,eadp5573(2024).DOI:10.1126/sciadv. adp5573

AJA Sputter 1 & 2 Materials Characterization

CNF Summer Student: Irwin Wang Student Affiliation: Department of Engineering, Cornell University

Summer Program(s): 2025 Cornell NanoScale Facility Research Experience for Undergraduates (CNF REU) Program Mentor(s): Tom Pennell, Cornell NanoScale Science and Technology Facility, Cornell University

Primary Source(s) of Research Funding: National Science Foundation under Grant No. NNCI-2025233,

Contact: iw87@cornell.edu, tjp83@cornell.edu

Abstract:

The application of sputtering for thin-film deposition has been a staple technique for decades, and its importance is growing with the expansion of nanotechnology. As new materials are developed to address unique challenges, their characterization within sputtering tools becomes increasingly essential. This study investigates the effects of various sputtering conditions on key film properties. The primary objective was to understand the relationship between sputtering parameters and both film Deposition Rate and Film Stress, while also measuring secondary characteristics such as Sheet Resistance and Index of Refraction. Depositions were performed using AJA 1 and AJA 2 Sputtering machines. The primary variable was chamber pressure, tested at three levels: 3 mTorr, 7 mTorr, and 20 mTorr. Deposition times were controlled to achieve a target film thickness between 100-300 nm for all samples. For a range of previously uncharacterized materials (Zr, Nb, Ru, Si3O4, Hf, NiO), trends for deposition rate and film stress were consistent with existing data. Specifically, increased chamber pressure generally resulted in a lower deposition rate. Film stress, as plotted and recorded against pressure, also matched general trends found with similar elements on other sputtering tools under different conditions. The key finding of this research was the consistency of these trends. The results suggest that the trends in film stress are element-specific and predictable. This research provides a foundation for future studies, allowing researchers to more accurately predict and plan for the effects of deposition parameters when working with novel materials

Summary of Research:

Sputtering is a common deposition technique used to create the thin films necessary for building devices. Materials are selected based on their desired electrical, physical, or chemical properties. To ensure these desired effects are achieved, a standard table of characterization data is crucial, especially since sputtering tools can differ from each other even under "identical" conditions.

Additionally, secondary effects like film stress are key considerations, as they can lead to device or film failure.

This research focused on collecting comprehensive data for a set of new materials on the AJA 1 and AJA 2 sputtering machines. The experimental process involved the following steps:

- 1. Wafer Preparation: Wafers underwent a MOS clean to remove organic contaminants and unwanted metals.
- 2. Native Oxide Removal: Prior to deposition, wafers were submerged in a two-minute buffered oxide etch to remove the native oxide layer.
- **3.** Deposition: Experimental conditions were varied, with deposition times estimated to achieve a target thin-film thickness of 100-300 nm.
- 4. Data Collection: A patterned chip, or "witness sample," was attached to the carrier during deposition. After liftoff, a profilometer was used to measure the film height, assuming uniform deposition. This data was then used to measure film stress using a Flexus tool. Additional measurements were taken using a four-point probe for sheet resistance and an ellipsometer for refractive index.

Conclusions and Future Steps:

Analysis of the data reveals consistent trends between sputtering pressure and the resulting film properties, particularly for deposition rate and film stress. For most materials, an increase in chamber pressure correlated with a decrease in deposition rate, a widely observed phenomenon in sputtering processes. Similarly, film stress exhibited predictable, element-specific responses to pressure changes, with a clear shift from tensile to compressive stress in several cases (e.g., Zr, Nb) and a general trend of becoming less compressive with increasing pressure (e.g., Si3N4, Hf, Ti). These consistent, predictable trends suggest that film properties can be reliably tuned by controlling chamber

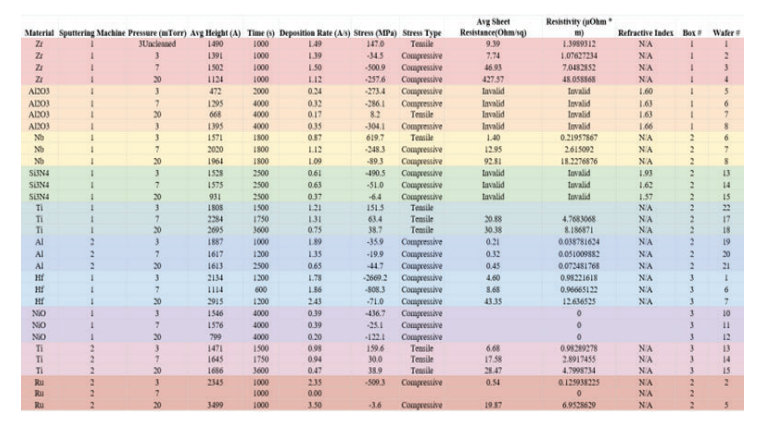


Figure 1.

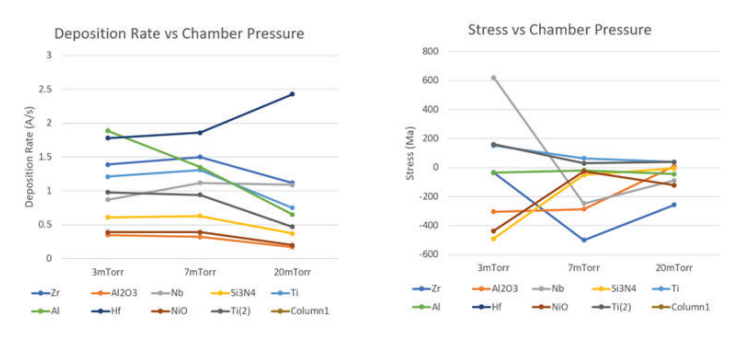


Figure 2.

pressure. The findings not only validate established sputtering principles but also provide a critical starting point for future researchers to optimize deposition conditions for a wide range of materials. In the future, this research hopes to expand its characterization by looking at film uniformity and roughness.

Acknowledgements:

Special thanks to Tom Pennell and the CNF staff for their support and mentorship throughout this whole research experience. I would like to acknowledge the CNF and their generosity for still offering a program after the 2025 AEOP program was canceled. This work was funded by the National Science Foundation via grants no. NNCI-2025233

Effects of Reactive Ion Etching on Conductivity of NbAs

CNF Summer Student: Iris You

Student Affiliation: Department of Materials Science and Engineering, Rutgers University

Summer Program(s): 2025 Cornell NanoScale Facility Research Experience for Undergraduates (CNF REU) Program, SUPREME REU

Principal Investigator(s): Judy J. Cha, Department of Materials Science and Engineering, Cornell University

Mentor(s): Yeryun Cheon, Department of Physics, Cornell University

Primary Source(s) of Research Funding: National Science Foundation under Grant No. NNCI-2025233, SUPREME Research Experience for Undergraduates #2349310

Contact: jc476@cornell.edu, yc2458@cornell.edu, icy2@scarletmail.rutgers.edu

Summer Program Website(s): https://cnf.cornell.edu/education/reu

Primary CNF Tools Used: Veeco Icon AFM, PT 720-740 RIE, Zeiss Supra SEM, Zeiss Ultra SEM

Abstract:

The continuation of Moore's Law has resulted in persistent downscaling of transistors and current copper (Cu) interconnects resulting in performance bottlenecks when interconnect dimensions are below the electron mean free path (~40 nm) of Cu [1]. Since Cu exhibits high resistance at such dimensionsscales, resistance-capacitance (RC) signal delay and high-power consumption result in lower overall performance [1]. Topological semimetals possess topologically protected conducting surface states that result in low resistivity at low dimensions [2]. Thus, they are of interest in the discovery of novel materials to replace Cu interconnects.

One such material is the Weyl semimetal niobium arsenide (NbAs). We have shown single crystal NbAs nanowires, produced by nanomolding, which has previously been shown to possess conductivity comparable to that of Cu at desirable length scales [3]. However, the promising resistivity trends of NbAs must be studied further as a function of size at sizes between these 10 nm and bulk crystals. has not been extensively studied aln addition, nd the effects of surface damage on conductivity due to various processing techniques has not been reported must be explored.

In this work, we use reactive ion etching (RIE) to reduce the size of focused ion beam (FIB) produced NbAs nanoscale samples prepared by focused ion beam (FIB) milling and examine the trends in resistivity as a function of NbAs size and RIE conditions. We show that NbAs can be etched roughly linearlycontrollably and reliably under mild RIE conditions and resistivity continuously decreases as NbAs is reduced in size. This allows for greater understanding of resistivity scaling and its mechanisms in NbAs.

Summary of Research:

We etched fabricated single crystal NbAs nanoslabs using FIB milling and created electrical devices. A completed device is shown in Figure 1. Length and width measurements were extracted from scanning electron microscopy (SEM) images. Atomic force microscopy (AFM) was used to measure the height of the slabs. The cross-sectional area of the slabs was calculated from this data. Resistance measurements were acquired via 4-point probe current and voltage measurements. The measured resistance was converted to resistivity When combined with dimensional data, we were able to calculate the resistivity of our NbAs slabsfor the NbAs slabs.

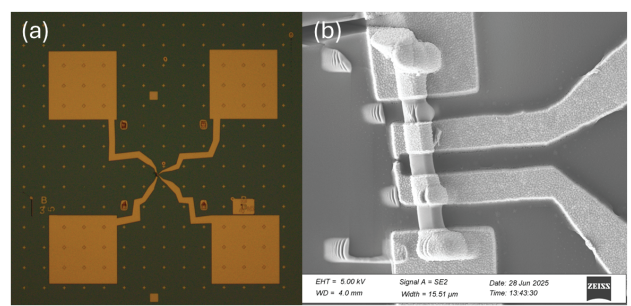


Figure 1: (a) Optical image of NbAs Device 3. (b) SEM image of Device 3.

The slabs were successively etched with RIE at 10 mTorr with 60 W of power using 30 sccm Cl₂ and 10 sccm CF₄ at varying etching times. Afterwards, AFM and resistance measurements were repeated to observe the changes in height and resistivity of the slabs. Figure 2 shows how uncertainty in the height measurements and thus etching calibration occurs due to the shape of the AFM tip as well as the geometry of the sample placed on the substrate. Additionally, we take into accountconsider the etching of the substrate when calculating the effects of etching. Overall, we are able to etched our devices at approximately 5-7 nm per minute.

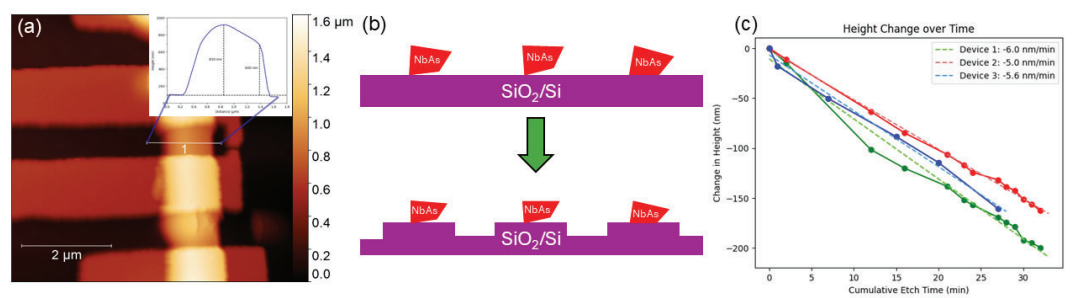


Figure 2: (a) AFM image with height profile of Device 3 pre-etching. (b) Schematic showing etching of substrate layer during RIE. (c) Plot of NbAs height change with respect to etching time.

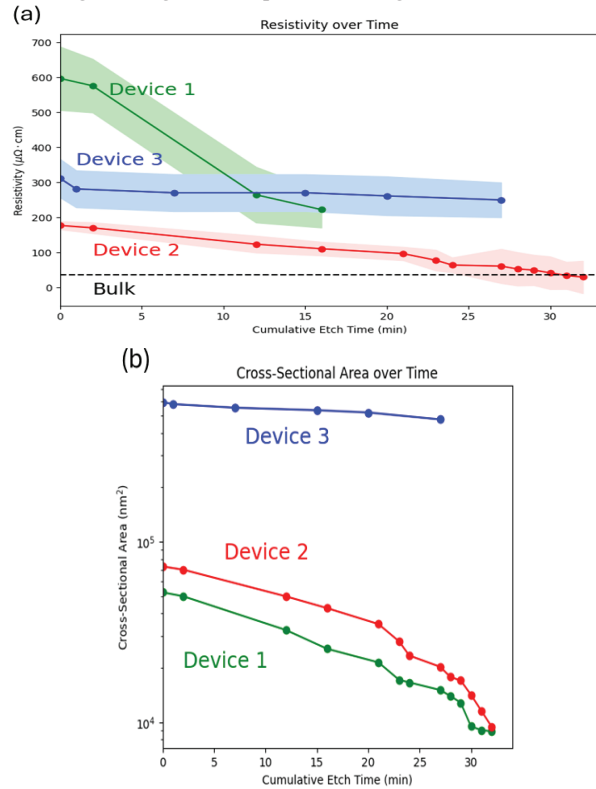


Figure 3: (a) Resistivity of NbAs devices as a function of total etch time. (b) Cross-sectional area of nanoslabs as a function of etch time.

There is a clear decreasing trend in resistivity as a function of cumulative etching time as shown in Figure 3. This supports the resistivity scaling trend of NbAs, and as the surface to volume ratio continuously increases from etching, the resistivity eventually falls below the bulk value while still decreasing.

SEM images in Figure 4 show considerable surface

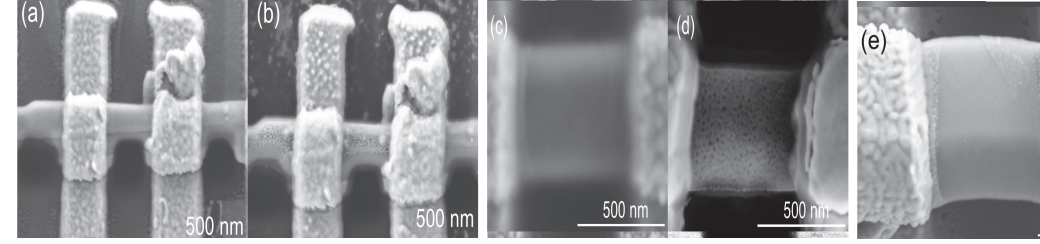
damage from RIE on the surface of the NbAs nanoslabs. However, the overall conductivity of the samples continues to exhibit decreasing behavior despite the surface damage.

Conclusions and Future Steps:

We progressively etched NbAs nanoslab devices through RIE at an etching rate of approximately 5-7 nm/min. We were further able to show that RIE is effective in reducing the size of NbAs without adversely affecting conductivity. We confirmed promising trend of decreasing resistivity for NbAs at decreasing dimensions in the nanoscale regime.

Future work would involve improving height measurements which are currently overestimated due to the geometry of the sample and FIB placement. Better methods to measure cross-sectional area would result in less overall error and a clearer understanding of our results. We would also like to continue investigating the surface contributions to the resistivity scaling of NbAs with RIE etching in future devices and investigate even less destructive methods of size reduction, whether it be through RIE or other means.

- Joon-Seok Kim et al., Addressing interconnect challenges for enhanced computing performance. Science 386, eadk6189 (2024). DOI:10.1126/science.adk6189
- [2] Asir Intisar Khan et al., Surface conduction and reduced electrical resistivity in ultrathin noncrystalline NbP semimetal. Science 387,62-67(2025). DOI:10.1126/science.adq7096
- [3] Cheon, Y et al. https://arxiv.org/abs/2503.04621 (2025).



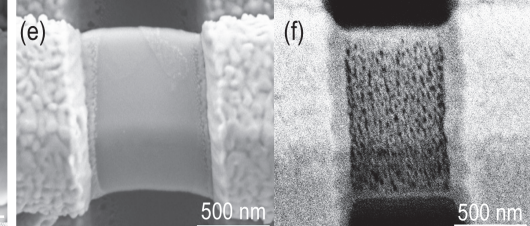


Figure 4: (a) Pre-etch SEM of Device 1. (b) Post-etch SEM of Device 1. (c) Pre-etch SEM of Device 2. (d) Post-etch SEM of Device 2. (e) Pre-etch SEM of Device 3. (f) Post-etch SEM of Device 3.

Synthesis of Temperature-Responsive Hydrogel Particles for Hydraulic Control of Cooled Short Circuits

CNF Project Number: 1356-05

Principal Investigator(s): Ulrich Wiesner

User(s): Danni Tang

Affiliation(s): Department of Materials Science and Engineering, Cornell University

Primary Source(s) of Research Funding: U.S. Department of Energy (DOE), Office of Energy Efficiency and Renewable

Energy (EERE), Office of Technology Development, Geothermal Technologies Program (DE-EE0009786.000)

Contact: ubw1@cornell.edu, dt427@cornell.edu

Research Group Website: http://wiesner.mse.cornell.edu/

Primary CNF Tools Used: Heidelberg DWL2000, ABM Mask Aligner, AMST MVD100, PDMS Station

Abstract:

Enhanced geothermal systems (EGS) offer a promising pathway for harvesting subsurface heat from previously unsuitable regions of the planet. Their operational efficiency, however, is often compromised by the occurrence of "short circuits", which arise from uneven permeability distributions within rock fracture networks. These short circuits can lead to preferential fluid flow through highly permeable regions, resulting in localized heat depletion, lower energy production efficiency, and even possible system failure. To mitigate this issue, temperature-responsive poly(N-isopropylacrylamide) (pNIPAM)-based hydrogel particles are designed to mitigate the issue by reducing the local permeability of "short circuit" regions. A parallel step emulsifier device is fabricated at CNF to produce particles with a narrow size distribution, and fundamental rheology tests will be conducted on the produced particles to understand their jamming behavior.

Summary of Research:

The "short circuit" issue arising from uneven permeability distributions within fracture systems is one of the major challenges in Enhanced Geothermal Systems (EGS). When a fluid gets injected underground, it preferably flows through highly permeable paths. As a result, these regions are rapidly drained of heat, leading to a premature thermal breakthrough and system failure [1]. To alleviate this problem, we designed temperature-responsive nanocomposite poly(N-isopropylacrylamide) (pNIPAM)-based microgel particles. As one of the most studied thermosensitive hydrogels, pNIPAM exhibits a reversible entropy-driven volume phase transition, leading to particle expansion at low temperatures and particle contraction at high temperatures [2]. With careful design, these pNIPAM-based particles can

expand to up to several hundred times their original volume when the temperature of their local environment falls below a threshold. This could effectively diminish short circuits by decreasing local channel permeability.

To produce thermo-responsive microgels with a narrow size distribution, a parallel step emulsifier was fabricated and optimized at the Cornell Nanoscale Science and Technology Facility (CNF). As of the last reporting period, we started the fabrication of the emulsifier device. Specifically, an emulsifier device adapted from Stolovicki et al. was produced at CNF (Figure 1) [3]. Photolithography was used to make the device master mold. The mold was subsequently used to pattern the final poly(dimethylsiloxane) (PDMS) based device. This device was expected to produce pre-gel droplets with a target size of around 30 μm. The droplets will then be polymerized under a UV source to form the final crosslinked polymer particles.

During this reporting period, our efforts have been focused on further optimizing the device fabrication and droplet production process. A key challenge we encountered in the previous fabrication attempts was the inconsistent bonding of nozzles to glass slides. As illustrated in Figure 2a, the previous bonding process involved first cutting the PDMS into the desired shape and then bonding it to the glass slides. The major issue with this method is that the PDMS is extremely deformable, and therefore even small deformations of the PDMS material can result in insufficient bonding of the channel to the glass substrate, which leads to polydisperse droplet production (Figure 3a).

To address this problem, a new bonding process has been developed. Here, instead of cutting the PDMS into its final shape and directly bonding it to the glass slides, we first cut and bond the whole molded PDMS slab with another plain PDMS slab. Then, we cut the assembled

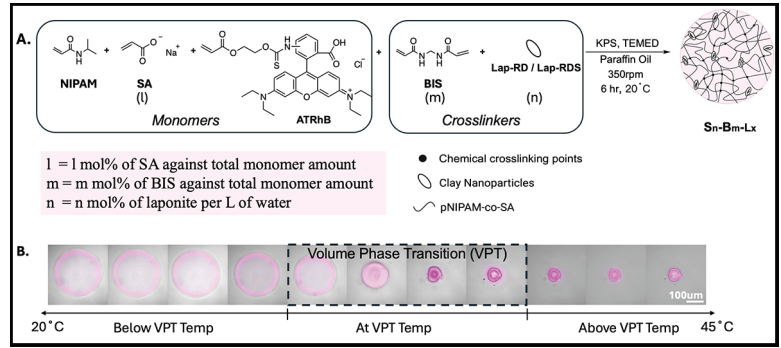


Figure 1: CAD design of the parallel step emulsifier device adapted from the Weitz group [1]. (A) Layer 1; (B) Layer 2; (C) merged images.

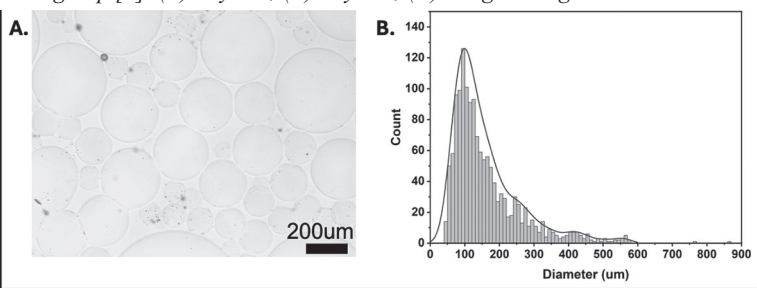


Figure 2: (A) Original PDMS device fabrication process (from the last reporting period) compared to optimized PDMS device fabrication process shown in (B).

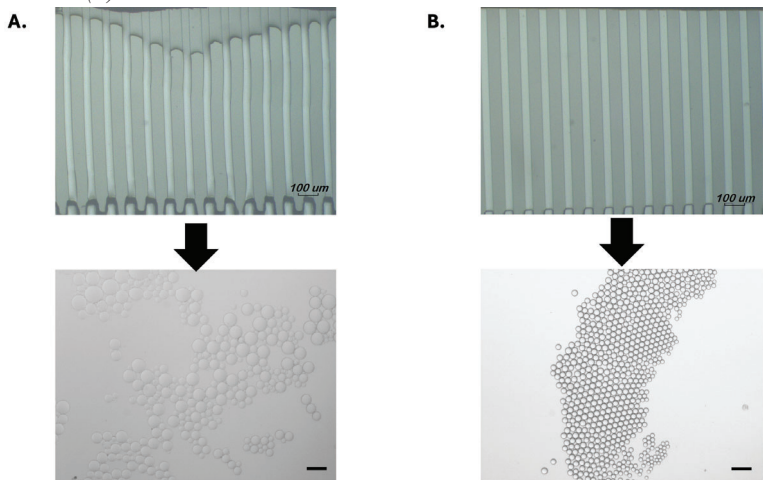


Figure 3: Typical optical images of the device nozzle areas (top) and resulting droplets (bottom) when using (A) the original PDMS device fabrication process (from the last reporting period) versus (B) the optimized PDMS device fabrication process. (Scale bar=100 μ m)

PDMS slabs into the final shape of the device and bond it to the glass slides (Figure 2b). This method significantly improves the nozzle bonding quality and allows better production of monodisperse droplets. As shown in Figure 3b, the produced particles exhibit significantly reduced size variation, indicating improved monodispersity.

Conclusions and Future Steps:

In conclusion, we have successfully fabricated a microfluidic device to produce temperature-response polymeric particles for geothermal applications. With further optimization in the PDMS binding process, we were able to produce droplets with narrow size distributions. In the next step, particles with varying compositions will be produced using this device and studied for their rheological behaviors.

- [1] Oh, K. W.; Lee, K.; Ahn, B.; Furlani, E. P. Design of Pressure-Driven Microfluidic Networks Using Electric Circuit Analogy. Lab Chip 2012, 12 (3), 515–545. https://doi. org/10.1039/c2lc20799k.
- [2] Hirotsu S.; Hirokawa, Y.; Tanaka, T. Volume-Phase Transitions of Ionized N-Isopropylacrylamide Gels. Journal of Chemical Physics 1987, 87 (2), 1392–1395. https://doi.org/10.1063/1.453267.
- [3] Stolovicki, E.; Ziblat, R.; Weitz, D. A. Throughput Enhancement of Parallel Step Emulsifier Devices by Shear-Free and Efficient Nozzle Clearance. Lab on a Chip 2017, 18 (1), 132–138. https://doi.org/10.1039/C7LC01037k.

Design and Synthesis of Sequence-Defined Oligopeptoids for Potential Lithographic Use

CNF Project Number: 175709

Principal Investigator(s): Christopher Ober

User(s): Danya Liu, Seungjun Kim

Affiliation(s): Materials Science and Engineering, Cornell University

Primary Source(s) of Research Funding: department of materials science and engineering, National Science

Foundation 23-552: Futre of Semiconductors (Fuse)

Contact: cko3@cornell.edu , dl957@cornell.edu, sk3434@cornell.edu

Research Group Website: https://ober.mse.cornell.edu/

Primary CNF Tools Used: AFM-Veeco Icon, ASML PAS 5500/300C DUV Wafer Stepper, and Woollam RC2

Spectroscopic Ellipsometer.

Abstract:

Extreme-ultraviolet (EUV) lithography underpins continued device miniaturization, yet conventional photoresists suffer from stochastic issues and the resolution-sensitivity-roughness trade-off at sub-10 nm dimensions.1, 2 Herein, we present a modular synthetic platform based on sequence-defined peptoids to overcome these limitations. In this work, two distinct oligopeptoid architectures were explored. The first employs a chemical amplification mechanism, using Boc-protected side chains to trigger solubility switching upon acid-catalyzed deprotection.3 Their lithographic performance, using either ionic or non-ionic photoacid generators (PAGs), was evaluated under deep-ultraviolet (DUV) exposure. The second is a creative innovation in which non-ionic PAGs were covalently tethered onto peptoid backbones via copper-catalyzed azide-alkyne cycloaddition, making the PAG itself the solubilityswitch moiety and ensuring uniform acid distribution.

Summary of Research:

We designed and synthesized bioinspired, sequencedefined and length-controlled oligopeptoids incorporating both clickable sites and solubility-switch functional groups. Two distinct strategies were explored: one employing Boc-protected tyramines as acid-labile switches in a chemically amplified resist system, and the other utilizing tethered non-ionic PAGs directly integrated into the peptoid backbone.

Thermal stability studies of both the oligopeptoids and PAG components helped determining the suitable postapply and post-exposure bake temperatures. Through systematic evaluation of key lithographic parameters—including developer composition, TMAH dilution ratios, and film thickness—a set of processing parameters was established to generate discernible patterns under

Figure 1: (a) Peptoid structure of PMFMPMFMP 9-mer, designed with propagyl amines as potential sties of click reaction and (b) PAG-incorporated peptoid by click reaction.

DUV exposure. Intriguingly, a tone-switch behavior was observed in peptoid films formulated with ionic PAGs, wherein thinner films behaved as positive-tone resists while thicker films as negative-tone, highlighting the complex interplay between film morphology and development responses.

Furthermore, a brand new type of resist using tethered PAG as the solubility switch was invented. The CuAAC click reaction was used to tether azide-functionalized PAGs onto peptoid backbones, with LC-MS confirming efficient tri-site conjugation under optimized reaction

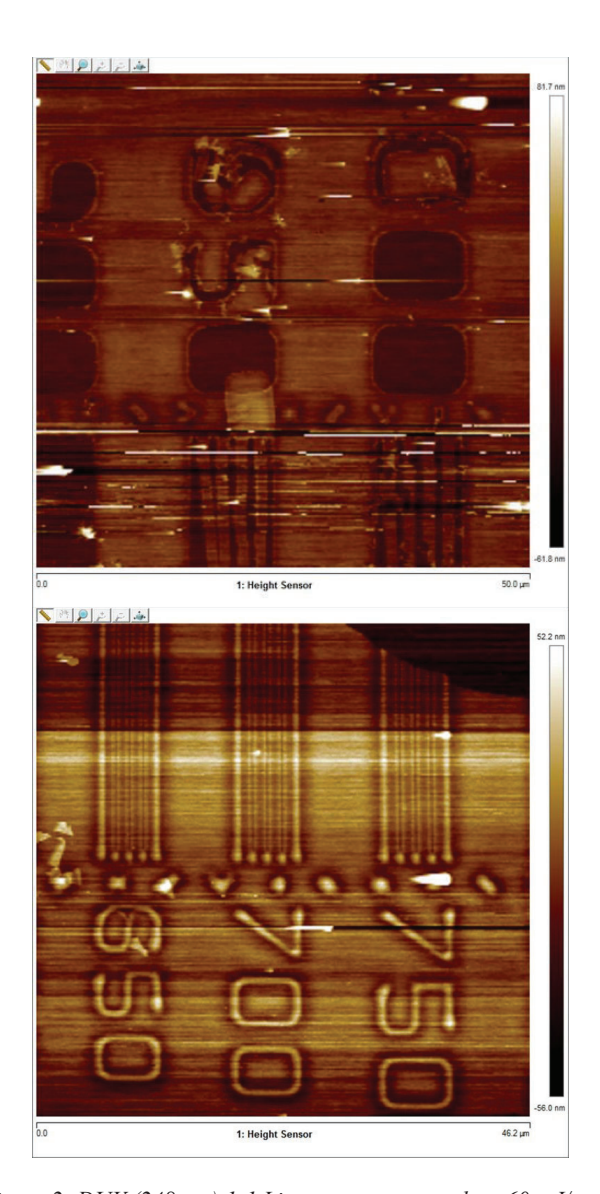


Figure 2: DUV (248 nm) 1:1 Line space pattern; dose 60 mJ/cm2; post-apply and post-exposure bake temperature 110 °C; 40 wt.% TPS-TF, developed in (a) undiluted AZ 726 for 3 seconds and (b) $50 \times \text{diluted AZ 726 for 45 seconds}$, observed under AFM.

conditions. Comparative evaluation of purification methods revealed that bypassing the alumina column step significantly improved overall yield particularly due to the low amount of copper catalyst content.

Overall, this study demonstrates a modular synthetic framework for peptoid-based photoresists with tunable chemical functionality and processibility, paving the way for further investigations into their performance under EUV and electron beam lithographic conditions, advancing the development of next-generation organic resist materials.

- [1] Enomoto, S.; Machida, K.; Naito, M.; Kozawa, T. In Study of RLS trade-off mitigation utilizing an organotin-containing chemically amplified resist for high sensitivity patterning, International Conference on Extreme Ultraviolet Lithography 2022, SPIE: 2022; pp 101-105.
- [2] Fonseca, C.; Head, B.; Shite, H.; Nafus, K.; Gronheid, R.; Winroth, G. In Understanding EUV resist dissolution characteristics and its impact to RLS limitations, Extreme Ultraviolet (EUV) Lithography II, SPIE: 2011; pp 343-353
- [3] Tarascon, R.; Reichmanis, E.; Houlihan, F.; Shugard, A.; Thompson, L., Poly (t-BOC-styrene sulfone)-based chemically amplified resists for deep-UV lithography. Polymer Engineering & Science 1989, 29 (13), 850-855.

Broadband Waveguide

CNF Project Number: 212612

Principal Investigator(s): Gregory David Fuchs

User(s): Srishti Pal, Qin Xu

Affiliation(s): Department of Applied Physics & Engineering and Department of Physics, Cornell University Primary Source(s) of Research Funding: Department of Energy (DOE) and Center for Molecular Quantum Transduction (CMQT)

Contact: gdf9@cornell.edu, sp2253@cornell.edu, qx85@cornell.edu

Research Group Website: https://fuchs.research.engineering.cornell.edu/

Primary CNF Tools Used: AJA Sputter Deposition, Heidelberg Mask Writer - DWL2000, GCA 6300 DSW 5X g-line Wafer Stepper, YES Asher, P7 Profilometer, Zeiss Supra SEM, Nabity Nanometer Pattern Generator System (NPGS), Dicing Saw - DISCO, Westbond 7400A Ultrasonic Wire Bonder.

Abstract:

We fabricate a broadband waveguide to test the magnetic properties of a low loss ferrimagnet vanadium tetracyanoethylene (V[TCNE]x) at cryogenic temperatures. We find that, in the temperature range between 0.44 K to 68.6 K, the linewidth of our V[TCNE] x sample increases with decreasing temperature. Below 0.44K, the resonance magnetic field decreases with decreasing temperature. These results are informative for the future applications of V[TCNE]x.

Summary of Research:

This research focuses on exploring exotic low-temperature broadband FMR response of the low-loss organic ferrimagnet V[TCNE]x.

The basic steps for patterning our broadband waveguide using photolithography are shown in Figure 1(a). First, we coat clean (with acetone followed by IPA) sapphire wafers with bilayer of LOR5A and S1813. The resist coated wafer is then exposed in 5X g-line Wafer Stepper to be patterned with the design written on a photomask using Heidelberg Mask Writer-DWL2000. The developed resist (in AZ726MIF) is descummed in YES Asher followed by deposition of 225 nm thick Ti/Cu/Pt tri-layer in the AJA sputter deposition tool. Finally, we lift-off the metal using 1165 and then dice the wafer using Dicing Saw-DISCO. For the magnon sub-system, we use the low-loss organic ferrimagnet V[TCNE]x with a low Gilbert damping $\alpha \sim 10-4$ offering long magnon lifetime and thus low Km. Using e-beam lithography in Nabity Nanometer Pattern Generator System (NPGS) connected to Zeiss Supra SEM, we pattern a 36 µm wide and 2 mm long bar on the 40 µm wide and 2 mm long central wire of the broadband chip using the steps shown in Figure 1(b). We then ship the exposed broadband chips to our collaborators in Ohio

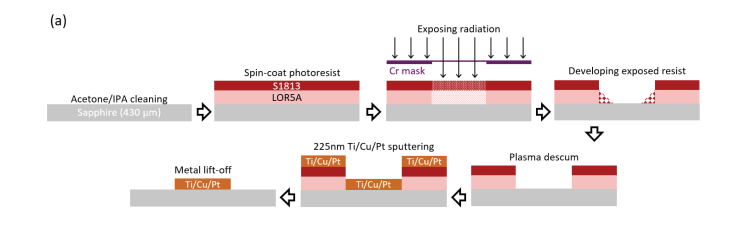


Figure 1: Process flow for (a) patterning the broadband chips with Ti/Cu/Pt tri-layer, and (b) e-beam patterning for V[TCNE]x deposition.

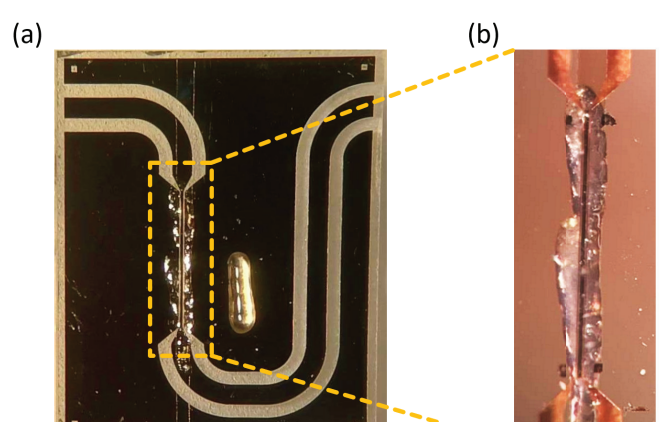


Figure 2: (a) Microscope image of broadband chip with patterned V[TCNE]x, ALD encapsulation, and protective grease layer. (b) Magnified microscope image of the region marked with yellow dashed rectangle in (a).

State University for V[TCNE]x growth and liftoff.

The V[TCNE]x is then encapsulated by ALD Alumina by our collaborators in Northwestern University to prevent degradation from air exposure and then sent back to us for measurement. We finally applied an additional layer of cryogenic grease for further protection of the V[TCNE]x film as shown in Figure 2.

For the FMR measurement setup, we first put the sample into a dilution refrigerator which has a base plate temperature of 15 mK. The broadband waveguide

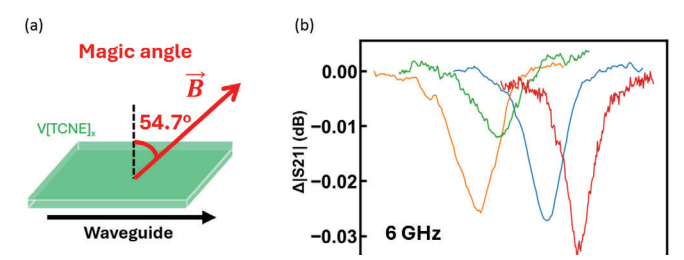


Figure 3: (a) Measurement setup scheme showing the orientation of the external field relative to the waveguide and the V[TCNE]x film. The external field is at 54.7•from the film normal of the V[TCNE]x film. (b) Microwave transmission spectrum vs the external magnetic field magnitude when the microwave frequency is 6 GHz. We can see the dip of the FMR resonance at different microwave excitation powers or temperatures. The 4 dips from left to right are obtained at -68 dBm microwave power at the sample in the dilution fridge; -58 dBm in the dilution fridge; -48 dBm in the dilution fridge; and -83 dBm at 0.44 K in the He-3 cryostat.

is connected to a vector network analyzer for the microwave transmission measurement. As shown in Figure 3(a), the external magnetic field is applied at 54.7• from the film normal (the magic angle) of the V[TCNE]x film. In this geometry, the inhomogeneous

linewidth caused by the length of the V[TCNE]x is minimized.

Figure 3(b) shows the 6 GHz microwave transmission magnitude vs the external magnetic field magnitude at different driving powers. When the V[TCNE]x's Larmor frequency matches 6 GHz, it will absorb some of the microwave energy, thus causing a dip in the transmission spectrum. The 3 dips on the left are the

transmission spectrums when the microwave powers at the sample are -68 dBm, -58 dBm and -48 dBm

respectively. The dip shifts to a higher magnetic field when the excitation power is higher, which is later shown to be caused by the heating of the V[TCNE] x. In other words, the dip shifts to a higher magnetic field when the sample temperature is higher. Note that this shifting happens at all directions of the external magnetic field, which rules out temperature dependent changes in magnetic anisotropy.

Then, the sample chip was put into a He-3 cryostat that has a tunable temperature between 0.44 K and 70 K. The rightmost dip in figure 3(b) is got when the sample space temperature is 0.44 K with –83 excitation power, which proves that the resonance field shift is caused by the raising temperature. Figure 4 shows the linewidth of the V[TCNE]x at 6 GHz and 14 GHz. It shows that the linewidth of V[TCNE]x increases with decreasing temperature. Also, most of the linewidth is due to frequency-independent broadening.

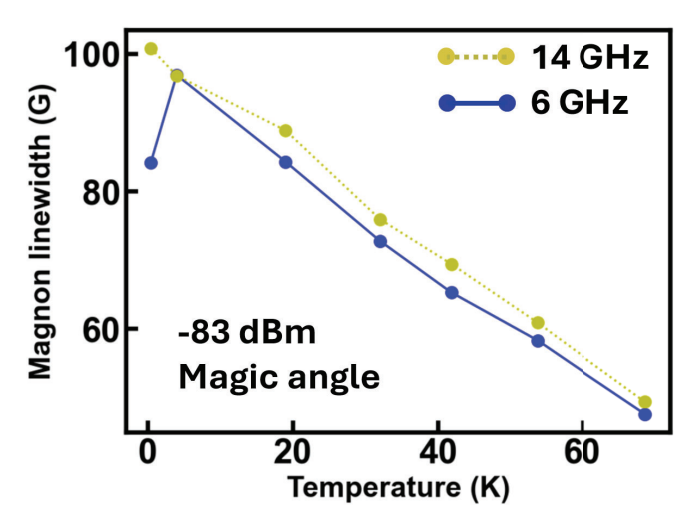


Figure 4: FMR linewidth of V[TCNE]x at 6 GHz and 14 GHz at different temperatures. The microwave power is -83 dBm.

Conclusions and Future Steps:

We fabricate a microwave frequency waveguide chip and use it to measure the broadband FMR of V[TCNE] x at cryogenic temperatures. We see an increase in FMR linewidth from 68.6 K to 0.44 K and a shift in resonance magnetic field vs temperature below 0.44K. More experiments are needed to fully characterize the sources of the observed linewidth and frequency changes.

- [1] H. F. H. Cheung, M. Chilcote, H. Yusuf, D. S. Cormode, Y. Shi, S. Kurfman, A. Franson, M. E. Flatté, E. Johnston-Halperin, and G. D. Fuchs, "Raman Spectroscopy and Aging of the Low-Loss Ferrimagnet Vanadium Tetracyanoethylene", The Journal of Physical Chemistry C 125, 20380 (2021).
- [2] Q. Xu, H. F. H. Cheung, D. S. Cormode, T. O. Puel, S. Pal, H. Yusuf, M. Chilcote, M. E. Flatté, E. Johnston-Halperin, and G. D. Fuchs, "Strong Photon-Magnon Coupling Using a Lithographically Defined Organic Ferrimagnet", Advanced Science 11, 2310032 (2024).

Sequence-Defined Polypeptoids Enable Stochastics Control and Discovery of Novel Patterning Mechanism in Next-Generation EUV Resists

CNF Project Number: 273318

Principal Investigator(s): Christopher Ober

User(s): Chenyun Yuan, Rika Marui

Affiliations(s): Department of Materials Science and Engineering, Cornell University

Primary Source(s) of Research Funding: Center for High Precision Patterning Science (CHiPPS), an Energy Frontier

Research Center funded by the U.S. Department of Energy.

Contact: cko3@cornell.edu, cy479@cornell.edu

Research Group Website: https://ober.mse.cornell.edu/

Primary CNF Tools Used: JEOL JBX-6300FS E-beam Lithography System, JEOL JBX- 9500FS E-beam Lithography

System, ASML DUV Stepper, AFM - Veeco Icon, Zeiss Gemini SEM

Abstract:

As lithography continues to advance into the extreme ultraviolet (EUV) regime, stochastic effects are becoming an increasingly significant challenge. One key contributor to it is the chemical stochastics, which arises from molecular-level inhomogeneities within photoresist materials. Traditional polymer-based photoresists often exhibit variations in molecular weight, composition, and sequence. In the case of chemically amplified resists (CARs), unbound photoacid generator (PAG) molecules may distribute unevenly at the nanoscale, and the lateral acid diffusion after exposure are somehow uncontrolled, further adding to stochastics. In this project, we investigated a photoresist system built on sequencedefined polypeptoids, which can be precisely tailored in terms of length, composition, and sequence, using the solid-phase submonomer synthesis method. These polypeptoid resists can be patterned in negative tone using either electron beam or EUV exposure, without requiring any additional photoactive components. This results in a monomolecular resist formulation that greatly minimizes chemical stochastic effects. We explored the patterning mechanism through a variety of characterization techniques and propose that the solubility behavior is driven by a mechanism that is rarely considered in EUV photoresist design. Additionally, we investigated how variations in composition and sequence affect lithographic performance, revealing consistent trends. With EUV exposure, we achieved a resolution of 14 nm half-pitch.

Summary of Research:

We have developed a novel sequence-defined polypeptoid photoresist platform to address stochastics challenges in

EUV lithography. Traditional polymeric photoresists struggle with chemical stochastics originating from the random nature of conventional polymers in terms of molecular weight, composition and sequence, as well as the random distribution of photoactive compounds and lateral acid diffusion in terms of CARs. There are also environmental concerns due to the use of PAGs which are mostly fluorinated compounds [1]. The new polypeptoid photoresist system, synthesized via solid-phase submonomer synthesis, features precisely positioned functional groups and exhibits uniform chain length, composition, and sequence [2-3]. These materials exhibit ultra-low dispersity and tunable properties, enabling intrinsic patternability under EUV and e-beam exposures without the need for PAGs. Their unique decarboxylation-based mechanism allows for high-resolution patterning (down to 14 nm half- pitch) and development in ultra-dilute (ppm level TMAH) or even aqueous developers, presenting a greener and more precise resist platform for next-generation lithography.

sequence-defined representative composed of six t-butyl ester and four phenol repeating units with a terminal carboxylic acid (Fig.1) was synthesized via solid-phase submonomer synthesis, purified by high-performance liquid chromatography (HPLC), and confirmed to be molecularly homogeneous by liquid chromatography-mass spectrometry (LC-MS). Its low molecular weight combined with a single molecular species enables high-resolution lithography. It is fully compatible with standard lithographic processes, forming homogeneous films via spin coating. Upon EUV or e-beam exposure, terminal carboxylic acids undergo decarboxylation, leading to CO2 outgassing and increased hydrophobicity. Patterns are developed without a post-exposure bake using a highly diluted (ppm-level) TMAH solution, or in some other sequences, deionized water, enabling an eco-friendly process.

These resists exhibit negative-tone behavior under both e-beam and EUV, and achieve resolutions 14 nm half-pitch under EUV (Fig. 2), demonstrating high patterning fidelity under both exposure methods. The decarboxylation-based mechanism has been confirmed with mass spectrometry analysis on post-exposure films and outgassing experiments.

Figure 1: Molecular structure of the example polypeptoid sequence.

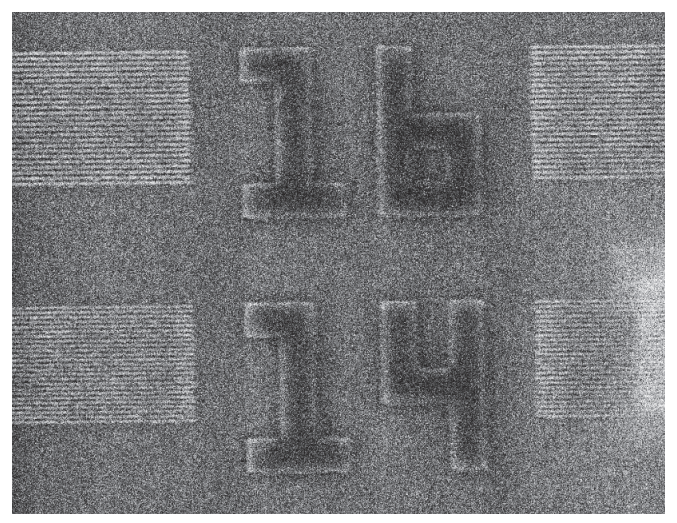


Figure 2: SEM image of EUV patterns showing 16- and 14-nm half-pitch line/space resolution.

Conclusions and Future Steps:

Our current research focuses on further improving patterning performance by screening libraries of selected polypeptoid sequences in which multiple carboxylic acid solubility-switch groups are positioned along the backbone, rather than one group exclusively at the chain end. We are also developing strategies to incorporate metal atoms with high EUV absorption into the polypeptoids to enhance sensitivity.

- [1] C. K. Ober, F. Käfer, J. Deng, Review of essential use of fluorochemicals in lithographic patterning and semiconductor processing. Journal of Micro/Nanopatterning, Materials, and Metrology 21, (2022). doi:10.1117/1.Jmm.21.1.010901
- [2] R. N. Zuckermann, J. M. Kerr, S. B. H. Kent, W. H. Moos, Efficient method for the preparation of peptoids [oligo(N-substituted glycines)] by submonomer solid-phase synthesis. J. Am. Chem. Soc. 114, 10646-10647 (1992). doi:10.1021/ja00052a076
- [3] C. P. Adams et al., Polymer Sequence Alters Sensitivity and Resolution in Chemically Amplified Polypeptoid Photoresists. ACS Macro Lett, 1055-1059 (2025). doi:10.1021/acsmacrolett.5c00320.

Two-Photon Printing of Polymer and Glass Electrospray Emitters

CNF Project Number: 295321

Principal Investigator(s): Elaine Petro, Sadaf Sobhani

User(s): Bryce Kingsley

Affiliation(s): Cornell University, Mechanical and Aerospace Engineering

Primary Source(s) of Research Funding: Government (DARPA)

Contact: epetro@cornell.edu, sobhani@cornell.edu, bjk234@cornell.edu

Research Group Website: https://www.sobhanilab.com, https://www.astralab.mae.cornell.edu

Primary CNF Tools Used: Nanoscribe GT2, Photolithography hoods, YES O2 Asher, DISCO Wafer Dicer

Abstract:

Advances in nano-scale additive manufacturing technologies have opened new possibilities for fabrication of precision components/parts with highly complex geometries. Within the field of space propulsion, these technologies are particularly relevant in the development and fabrication of electrospray thrusters - propulsion systems which utilize charged droplet/ ion emission for thrust generation. A fundamental component of these thruster systems is the electrospray emitter, wherein performance depends heavily on the resolution and geometrical characteristics of the emitter structure. Conventional fabrication processes (MEMS techniques, micromachining, etc.) often lack the resolution, geometric flexibility, or material compatibility needed for optimal emitter design and fabrication. This work investigates an alternative technique of electrospray emitter fabrication using Two-Photon Polymerization printing, exploring its potential to produce intricate emitter architectures and integrated microfluidic structures that can enhance the performance of electrospray thrusters.

Summary of Research:

Two-Photon Polymerization (TPP) printing an emerging nano-scale additive manufacturing process which utilizes a high-power laser to print 3D structures from photosensitive resin. Figure 1 shows a generalized schematic of a TPP printing system. A NIR (near infrared) laser is projected through a microscope objective and focused within a pool (dip) of photosensitive resin. Two-photon absorption near the focal region of the beam elevates the energy above the activation energy of the resin, resulting in cross-linking and solidification of the resin into a solid feature. Using precise positioning systems, the beam is drawn in XYZ space to fabricate 3D parts/components. In this work, we utilize the Nanoscribe Photonic Professional GT2 printer available in the CNF facilities. Using the GT2 system, we fabricate electrospray emitters from polymer (IP-Q) and glass (GP-Silica and POSS) resins.

The user-friendly nature of the GT2 printing system greatly simplifies the emitter fabrication process, as follows: (1) the emitter geometry is modeled using standard CAD software and exported to a mesh, (2) the emitter mesh is sliced using Nanoscribe's slicing software (Describe) and transferred to the GT2 system for printing, (3) a clean substrate (silicon) is loaded into the printer with the selected photosensitive resin (polymer/ glass), (4) emitter geometry is printed (typically <10 minutes), (5) substrate and emitter removed from GT2 and developed to remove residual resin, and (6) thermal post-processing (glass resins only). This simplified fabrication process promotes rapid prototyping and development of novel emitter designs which would be difficult with conventional methods, such as chemical etching which would require multiple stages of etching and new masks developed for each new prototype [1]. Additionally, TPP printing enables emitter architectures that would be extremely challenging or impossible to achieve with traditional fabrication techniques. We leverage this capability by integrating microfluidic channels and structures within the body of the printed emitters to promote propellant transport to the emitter tip and improve performance. One such microfluidic structure we implement is the Triply-Periodic Minimal Surface (TPMS), which is a lattice structure that is generated from 3D mathematical equations. Figure 2 contains an SEM image of a polymer (IP- Q) emitter printed with the gyroid TPMS lattice structure. This structure contains a network of interconnected micropores (~8 µm) for propellant to transport from the base (where it is loaded) to the tip (the site of emission). We note that this work uses the 10X microscope objective for printing, which has a minimum TPMS pore size of approx. 6 µm. A higher objective (e.g., 25X) would be required for smaller pores, at the expense of longer print times.

As mentioned previously, glass emitters are fabricated using TPP printing with specialized photosensitive resins. Here, we use two formulations of glass resins:

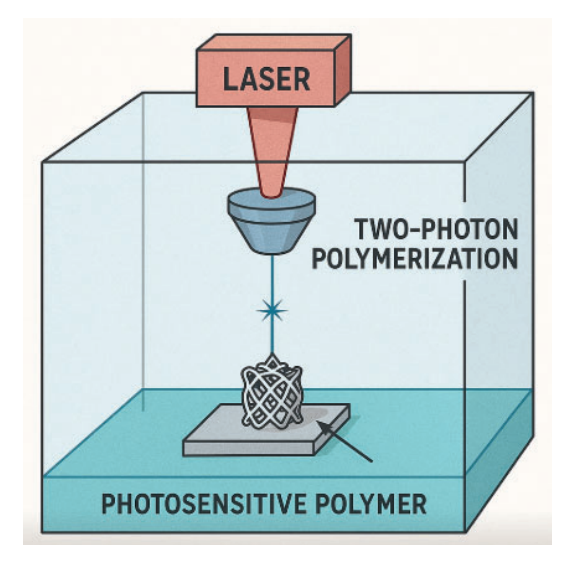


Figure 1: Schematic of two-photon polymerization (TPP) printing.

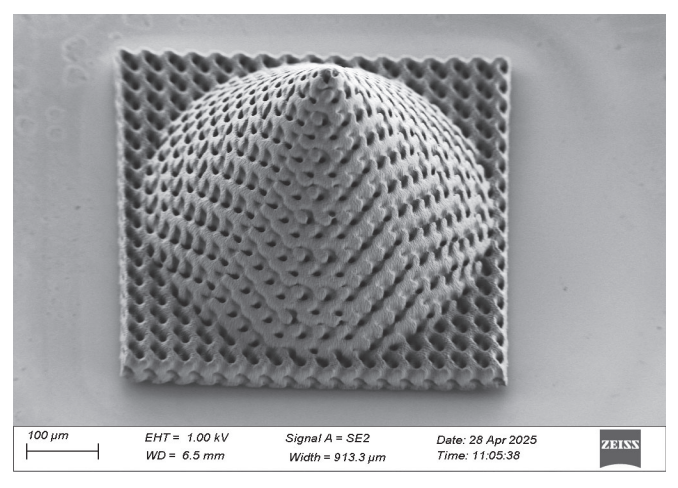


Figure 2: SEM of a polymer electrospray emitter TPP-printed with a TPMS lattice structure.

(1) the GP-Silica resin from Nanoscribe which contains silica nanoparticles that fuse together during thermal treatment, and (2) a POSS (polyhedral oligomeric silsesquioxane) formulation which chemically transforms into fused silica during thermal treatment [2]. For the application of electrospray emitters, glass/ fused silica is advantageous over polymer materials due to its higher degree of wettability and stability (chemical, thermal, etc.). Figure 3 contains 3D optical profilometry scans of a TPP-printed glass emitter before (a) and after (b) thermal post-processing. As can be seen in the profilometry scans, thermal processing introduces significant shrinkage (~35-40%) of the emitter structure which must be accounted for during the design stage to achieve accurate geometry/dimensions.

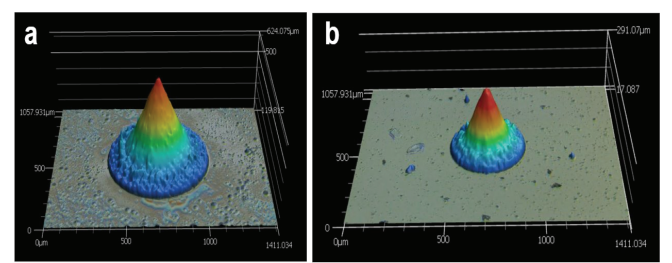


Figure 3: 3D optical profilometry scan of a TPP-printed glass emitter (a) before and (b) after thermal treatment.

Conclusions and Future Steps:

This work investigates a new/alternative technique of fabricating electrospray emitters using two-photon polymerization (TPP) printing. The unique capabilities and advantages of TPP printing enable highly complex emitter architectures that would be very challenging or impossible to fabricate with traditional emitter fabrication processes. Microfluidic channels and structures (TPMS) can be integrated directly into the body of the printed emitters to tailor fluid/propellant transport to the tip for optimized emission. TPP printing supports different materials systems, enabling emitters to be fabricated out of polymer or glass materials.

This work is ongoing and testing is currently underway to evaluate the emission performance of these printed emitters compared to standard electrospray emitters. Additionally, we have plans to scale-up to fabricating emitter arrays (i.e., gridded emitters) for implementation in electrospray thruster systems.

- [1] L. F. Velasquez-Garcia, A. I. Akinwande and M. Martinez-Sanchez, "A Planar Array of Micro-Fabricated Electrospray Emitters for Thruster Applications," Journal of Microelectromechanical Systems 15, 1272-1280 (2006), DOI: 10.1109/JMEMS.2006.879710
- [2] J. Bauer, C. Crook and T. Baldacchini, "A sinterless, low-temperature route to 3D print nanoscale optical-grade glass," Science 380, 960-966 (2023), DOI: 10.1126/science.abq3037.

A Brief Survey of Contact Angle Measurements for Predicting Fluid Flow in Electrospray Emitters

CNF Project Number: 295321

Principal Investigator(s): Sadaf Sobhani

User(s): Lindsay Wright

Affiliation(s): Sibley School of Mechanical and Aerospace Engineering

Primary Source(s) of Research Funding: RA Offer for the Defense Advanced Research Projects Agency, Account

#E559359

Contact: sobhani@cornell.edu, law289@cornell.edu

Research Group Website: sobhanilab.com

Primary CNF Tools Used: VCA Optima Goniometer, spincoating fume hoods

Abstract:

Electrospray is a method of satellite propulsion and mass spectrometry that works by moving ionic liquid from a receptacle to emitter tips and then vaporizing and propelling the ions using strong alternating electric fields from an extractor. With recent advances in additive manufacturing, electrospray emitters can be custom manufactured for different surface properties to optimize fluid flow. However, fluid flow in electrospray emitters has mainly been parametrized using metrics such as permeability or impedance, without the level of detail necessary to design channel networks. Our work aims to model the effects of specific materials and surface treatments on the speed of fluid flow—to

develop an accurate predictive framework, a study of different materials' surface properties is necessary. Thus, a series of samples have been fabricated in the Cornell Nanoscale Facility to obtain contact angle measurements.

Summary of Research:

Two Photon Polymerization was attempted to create contact angle measurements that matched the surface characteristics of additively manufactured electrospray emitters. Due to bumps and other surface texture discrepancies caused by stitching in larger print sizes, we opted for spin coating surfaces instead, curing them under UV to replicate the Two Photon Polymerization process with a more even surface.

The following recipes were created for spin coating:

GP Silica: Dispense approximately 1 mL of resin on 1" silicon wafer square. Then, ramp to 500 rpm at 100 rpm/sec, and hold for 5-10 seconds. Next, ramp to 1000 rpm/s at a rate of 300 rpm/sec, and hold for 30 seconds. Finally, soft bake for 6 mins at 65 degrees Celsius, then 20 mins at 95 degrees Celsius

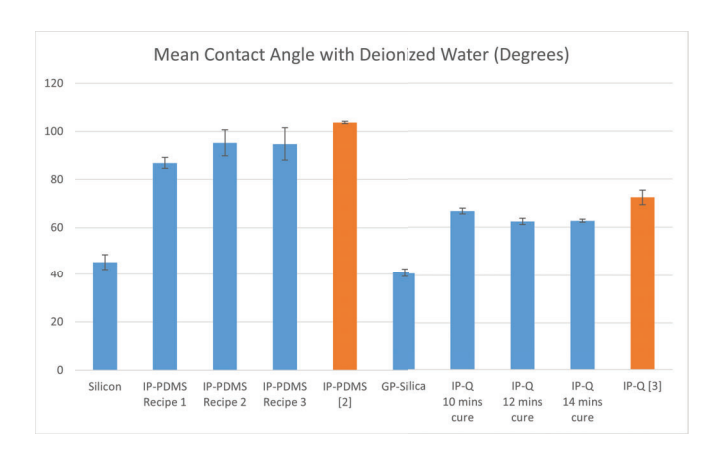


Figure 1: Contact Angles of Spin Coated Polymer Resin Recipes with Deionized Water

IP-PDMS Recipe 1 (created by collaborator at Rice University): Dispense approximately 1 mL of resin on 1" silicon wafer square. Next, ramp at 10 rpm/s to 500 rpm, and hold for 5 seconds. Finally, UV cure the sample for 10 minutes using an Aiffoto brand lamp [1].

IP-PDMS Recipe 2: Dispense approximately 1 mL of resin on 1" silicon wafer square. Next, ramp at 10 rpm/s to 500, and hold for 5 seconds. Then, UV cure samples for 30 minutes using the cylinder lamp at the Cornell Nanoscale Facility, reported to have an energy flux of 21 mW/cm² @ 405nm

IP-PDMS Recipe 3: Prime a 1" silicon wafer with 20% HMDS (first at 700 rpm, with a 1000 rpm/s ramp at 10 seconds duration; then, at 2500 rpm, with a 1000 rpm/s ramp and 60 seconds duration). Then, dispense approximately 1 mL of resin on 1" silicon wafer square. Ramp the spin coater at 10 rpm/s to 500 rpm and hold for 5 seconds. Next, UV cure samples for 30 minutes using the cylinder in the Cornell Nanoscale Facility. Finally, develop for 10 minutes in isopropanol.

IP-Q: Prime a 1" silicon wafer with 20% HMDS. Then,

dispense approximately 1 mL of resin on 1" silicon wafer square. Ramp to 500 rpm at 100 rpm/sec and hold for 5 seconds. Next, ramp to 2500 rpm at 300 rpm/sec, for a total of 40 seconds. Then, UV cure samples to the desired time (10, 12, or 14 minutes) using the Cornell Nanoscale Facility lamp.

Finally, develop for 10 minutes in isopropanol.

Contact angle measurements of varying surface recipes with deionized water were measured with a Ramehart 500 Goniometer, except for IP-PDMS samples fabricated using Recipes 2 and 3, which were measured by processing iPhone 16 images with ImageJ. The data with standard error bars can be found in Figure 1, along with literature values for IP-PDMS and IP-Q to compare [2] [3].

Apreliminary study of the contact angle measurements of ionic nanoparticle fluids suspended in polymer matrices was also conducted for silicon and IP-PDMS. Silicon had a contact angle of 48.3 degrees with water, 17.6 degrees with Jeffamine, and 13.4 degrees with NIMS 15 2:1, while Recipe 1 for IP-PDMS had a contact angle of 90.7 degrees with water, 37.7 degrees with Jeffamine, and 64.2 degrees with NIMS 15 2:1.

Conclusions and Future Steps:

A majority of the polymer resins used were weakly hydrophilic to water. GP-Silica, due to being a glass resin, is more strongly hydrophilic, while IP-PDMS is borderline hydrophobic. It will be interesting to continue to study the properties of ionic liquids and ionic nanoparticle fluids against different surfaces to determine whether more complex interactions are occurring that influence wettability.

IP-PDMS and IP-Q contact angle measurements were found to be consistently more hydrophilic than literature values, with the difference between literature and observations being more pronounced in IP-PDMS samples. It is noted that Govindarajan et al cured IP-PDMS using a 10W 395nm wavelength lamp [2]. Isaakidou used Two Photon Polymerization with a center wavelength of 780 nm, operating at 80 MHz at a duration of 100 fs to fabricate IP-Q samples [3]. The degree to which these differences affect the contact angle is a point to investigate.

A preliminary study of UV cure time and contact angle measurements was made for IP-Q, with the contact angle decreasing slightly over time from 10 to 12 to 14 minutes. Future steps would include experimenting with different treatments in addition to UV cure time. Experimentalists have found, for example, that UV-

ozone treatment of PDMS can reduce the contact angle at controllable rates, which could be preserved by storage in distilled water [4]. Additional surface treatments could include etching, Atomic Layer Deposition, and Molecular Vapor Deposition to further manipulate the surface.

- [1] Amazon (n.d.). 3D Printing UV Resin Curing Light 405nm, Smart 3D Printer UV Resin Curing Light for Solidify Photosensitive Resin, Portable Timer Function DIY Curing Enclosure, 5V/2A Input USB Powered. https://www.amazon.com/dp/B0D5HKQ2DQ?ref_=ppx_hzsearch_conn_dt_b_fed_asin_title_1
- [2] Isaakidou, Aikaterini, Iulian Apachitei, Lidy Elena Fratila-Apachitei, and Amir Abbas Zadpoor. 2023. "High-Precision 3D Printing of Microporous Cochlear Implants for Personalized Local Drug Delivery" Journal of Functional Biomaterials 14, no. 10: 494. https://doi. org/10.3390/jfb14100494
- [3] Srinivasaraghavan Govindarajan, Rishikesh & Sikulskyi, Stanislav & Ren, Zefu & Stark, Taylor & Kim, Daewon. (2023). Characterization of Photocurable IP-PDMS for Soft Micro Systems Fabricated by Two-Photon Polymerization 3D Printing. Polymers. 15. 10.3390/ polym15224377.
- [4] Kun Ma, Javier Rivera, George J. Hirasaki, Sibani Lisa Biswal, Wettability control and patterning of PDMS using UV–ozone and water immersion, Journal of Colloid and Interface Science, Volume 363, Issue 1, 2011,Pages 371-378, ISSN 0021-9797, https://doi.org/10.1016/j.jcis.2011.07.036.

Lithography on 2D Materials for Stressor Film Deposition

CNF Project Number: 296721

Principal Investigator(s): Judy Cha

User(s): Sihun Lee, Yu-Mi Wu

Affiliation(s): Department of Materials Science and Engineering, Cornell University

Primary Source(s) of Research Funding: The Gordon and Betty Moore Foundation's EpiQS Initiative (GBMF9062.01);

Department of Energy, Basic Energy Sciences program Grant No. DE-SC0023905

Contact: jc476@cornell.edu, sl2859@cornell.edu, yw2658@cornell.edu

Research Group Website: https://cha.mse.cornell.edu

Primary CNF Tools Used: Heidelberg MLA 150 Maskless Aligner, SC4500 Evaporator, Zeiss Supra scanning electron

microscope, Nabity Nanometer Pattern Generator System

Abstract:

To investigate the heterostrain-induced electronic properties in 2D materials, we fabricated stressor thin film Al2O3/SiO2/Al2O3 directly onto the target materials using lithographic patterning. Direct writing lithography tools were used to pattern the resist with stripes, followed by thin film deposition of stressors using e-beam evaporation. Subsequently, metal contacts were integrated for device characterization, revealing the effects of strain on the structural and electrical transport properties of MoS2.

Summary of Research:

Recent experimental advances in process-induced strain-engineering technique have enabled controlled strain application in 2D materials through lithographic patterning of stressor thin films [1], providing a versatile platform to engineer material properties. Here, utilizing the process- induced strain-engineering approach [2], we apply heterostrain to exfoliated MoS2 flakes by patterning evaporated thin film stressors, and fabricate biasing devices to characterize their resulting strain-induced electrical properties of MoS2.

The biasing devices were fabricated on conventional Si/SiO2 substrates. Figure 1 shows a cross- sectional schematic of the device design and a plan-view optical image of the device used for electrical transport measurements. First, the interdigitated electrode design with a 1 µm spacing, was patterned directly onto a Si/SiO2 substrate using photolithography with the MLA 150 direct writer. Cr/Au contacts were subsequently deposited using e-beam evaporation, followed by a lift-off process. Subsequently, the exfoliated MoS2 flakes were transferred onto the pre-patterned electrodes using a conventional polymer-assisted dry transfer technique. To introduce the local strain, the MLA 150 was used again to pattern a small stripe on top of the MoS2 flake

(highlighted in red), where the Al2O3/SiO2/Al2O3 stressor films were deposited via e-beam evaporation. The draw-mode functionality of the MLA 150 facilitates the stressor patterning process without requiring any additional alignment steps, ensuring accurate overlay with the target flake region.

To investigate the structural effects of heterostrain at high resolution, we also fabricated samples on transmission electron microscopy (TEM) grids with freestanding membranes. Figure 2 shows optical images of the TEM grid overview and the fabrication process. Poly(methyl methacrylate) was used as the resist, and the patterning was conducted using e-beam lithography with the Nabity Nanometer Pattern Generator System on the Zeiss Supra scanning electron microscope. Manual alignment was employed to center the stripe patterns (~10 µm in width and spacing) onto the membrane region of the TEM grids. Following exposure, Al2O3/ SiO2/Al2O3 stressor films were deposited via electron beam evaporation. The stripe-patterned stressor films were successfully deposited directly onto MoS2 flakes on the TEM grids, enabling subsequent structural characterization.

Next step, we investigated the local structural changes induced by heterostrain in MoS2 using scanning transmission electron microscopy (STEM). Figure 3 focus on a MoS2 flake under the patterned film stressor on the TEM grid. The white dotted line marks the boundary where the stressor film terminates. As shown in Fig. 3b and 3c, dislocations appear as bright lines in the low- angle annular dark-field STEM images due to the diffraction contrast. The observed diamond- shaped dislocation network in MoS2 likely originates from heterostrain-induced lateral displacement between layers. The strain transferred from the stressor film is primarily applied to the topmost few layers of MoS2, resulting in interlayer sliding and modified stacking

configurations. This sliding induces a dislocation network that relieves the resulting lattice mismatch and reflect local structural relaxation mechanism in the system.

Conclusions and Future Steps:

DLS is a facile tool to characterize the emulsion condition of colloidal system. For emulsions with nanoparticles and multiple ingredients, it's a challenge to make ideally uniform nano-encapsulation environments. Concentration and temperature play critical roles and need to be modified systematically in the future.

- Chenyun Yuan, Florian Kafer, and Christopher K. Ober. (2021). Polymer-Grafted Nanoparticles (PGNs) with Adjustable Graft-Density and Interparticle Hydrogen Bonding Interaction.
- [2] Alicia Cintora, Florian Kafer, Chenyun Yuan, and Christopher K. Ober. (2021). Effect of monomer hydrophilicity on ARGET-ATRP kinetics in aqueous mini-emulsion polymerization.
- [3] Roselynn Cordero, Ali Jawaid, Ming-Siao Hsiao, Zoe Lequeux, Richard A. Vaia, Christopher K. Ober, "Mini Monomer Encapsulated Emulsion Polymerization of PMMA in Aqueous ARGET ATRP", ACS Macro Letters, 7, 4, 459-463.

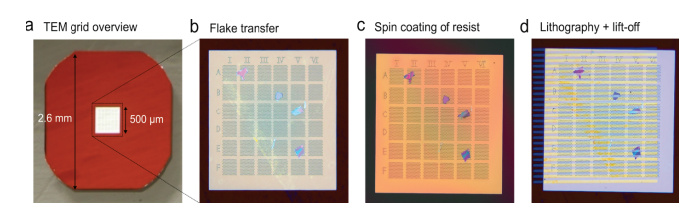


Figure 2: (a) Overview of the TEM grid with a 500 µm x 500 µm membrane where the material can be imaged with a TEM. (b-d) Zoomed-in images of the MoS2 flakes transferred onto a TEM grid, followed by the spin coating of the PMMA resist, then e-beam lithography patterning and lift-off, respectively. Stripes of the stressor film Al2O3 (10 nm)/SiO2 (30 nm)/Al2O3 (10 nm) are deposited on top of the MoS2.

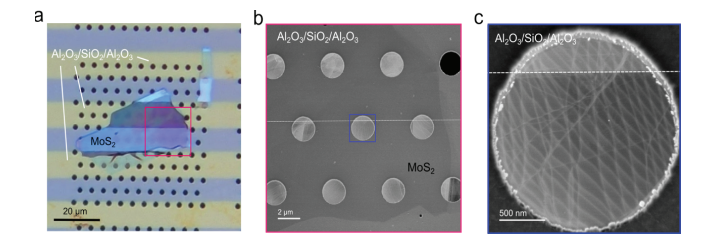


Figure 3: (a) An optical image showing a single MoS2 flake partially covered by a stressor film (yellow region on the TEM membrane). (b) Low magnification low-angle annular dark-field (LAADF) scanning transmission electron microscopy (STEM) image of MoS2 from the red box in (a). (c) LAADF STEM image of MoS2 over a single membrane hole from the blue box in (b), showing dislocations from the diffraction contrast.

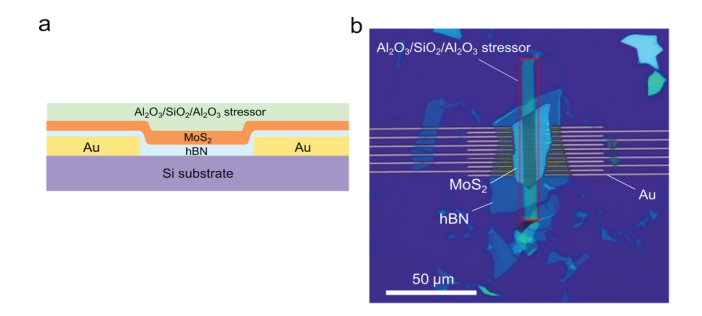


Figure 1: Figure 1. (a) Cross-sectional schematic of the device with stressor film. (b) Optical image of a biasing device fabricated for electrical transport measurements. The red outline shows where the stressor film was deposited. The MoS2 sits above the biasing electrodes and an insulating dielectric hBN layer.

Area Selective Deposition

CNF Project Number: 299021

Principal Investigator(s): James R. Engstrom

User(s): James T. Jensen, Jay V. Swarup

Affiliation(s): Chemical Engineering, Cornell University

Primary Source(s) of Research Funding: DOE

Contact: jre7@cornell.edu, jtj33@cornell.edu, jvs64@cornell.edu

Primary CNF Tools Used: Woollam RC2 Spectroscopic Ellipsometer, VCA Contact Angle, Oxford FlexAL

Abstract:

In this work, we describe our results aimed at developing the fundamental framework behind the use of small molecules to achieve area selective deposition (ASD), examining the atomic layer deposition (ALD) of Al2O3 on SiO2. We have examined 2 precursors, and 2 blocking molecules. For ASD, we have determined that the size of the precursor and blocking molecule strongly influence blocking efficacy, with bulkier precursors and long-chain self-assembled monolayers (SAM's) leading to increased blocking on SiO2.

Summary of Research:

We are developing the fundamental framework behind the use of small molecules to achieve ASD, examining the deposition of Al2O3 on SiO2. The overall approach is to examine explicitly the effects of the choice of the precursor and blocking molecules on blocking Al2O3 thin film growth on SiO2.

We have employed a quartz crystal microbalance (QCM) to monitor thin film deposition in situ and in real-time.1,2

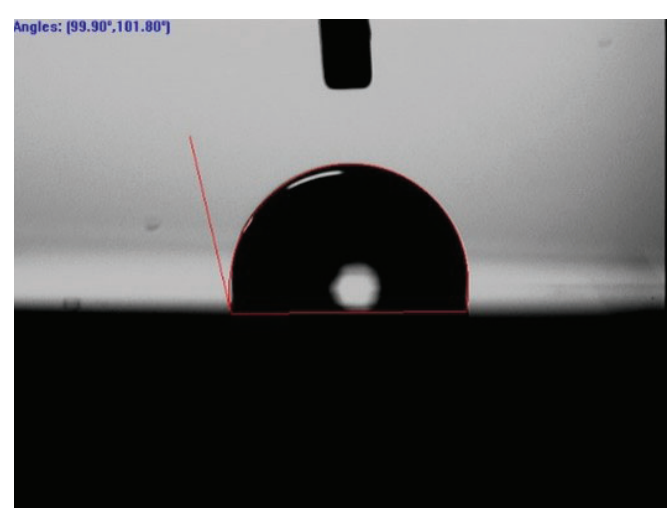


Figure 1: Water contact angle of DMATMS-passivated SiO2 is ~95°, which is significantly higher than Bare SiO2 which is ~15°.

In CNF, we coated Au QCM crystals with 20 nm of SiO2 to get a starting surface of SiO2 for ASD experiments. We exposed the SiO2 surface to the blocking molecule: (N.N-dimethylamino)trimethylsilane (DMATMS) in vapor phase and octadecyltrichlorosilane (ODTS) in solution phase. Water contact angles were used to assess changes in surface chemistry. The SiO2 surface becomes hydrophobic upon formation of the blocking molecule, and these changes are shown in Figures 1 and 2. Once the blocking molecule was formed, we performed ALD in our laboratory using 2 different precursors: trimethylaluminum (TMA) and bisdimethylaminodiamino-Aluminum (BDMADA-Al). A key difference between these precursors is that BDMADA-Al is larger and bulkier due to its more complex ligands compared to TMA. In Figure 3 we show QCM data for 40 cycles using BDMADA-Al as the precursor and H2O as the co-reactant at T = 120 °C on ODTS- and DMATMS-SiO2 QCM crystals. From the QCM results, the longer-chain ODTS blocking molecule resulted in prolonged attenuation of growth on SiO2. In Figure 4 we show a similar set of experiments but using TMA as the precursor. From these results, we again see longer attenuation of growth on ODTS compared to DMATMS, although the growth is larger than what was observed using BDMADA-Al as the precursor under

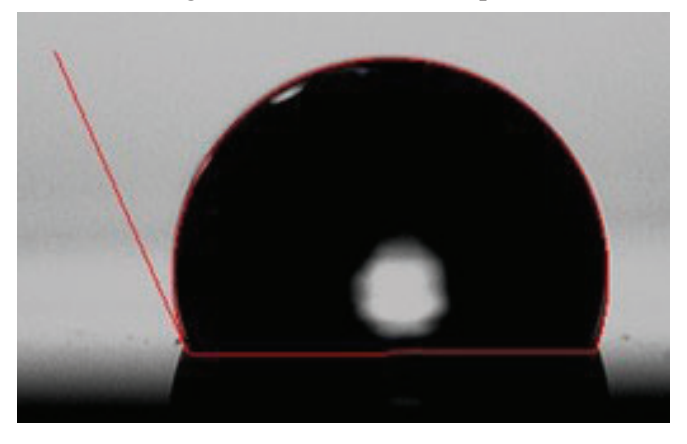


Figure 2: Water contact angle of ODTS-passivated SiO2 is ~110°, which is significantly higher than Bare SiO2 which is ~15°.

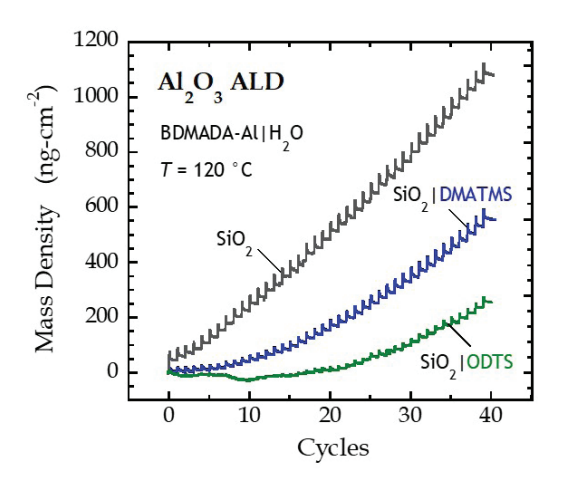


Figure 3: QCM data showing mass densities vs number of cycles for Al2O3 using BDMADA- Al|H2O process chemistry at T=120 °C on SiO2 crystals passivated with either DMATMS or ODTS.

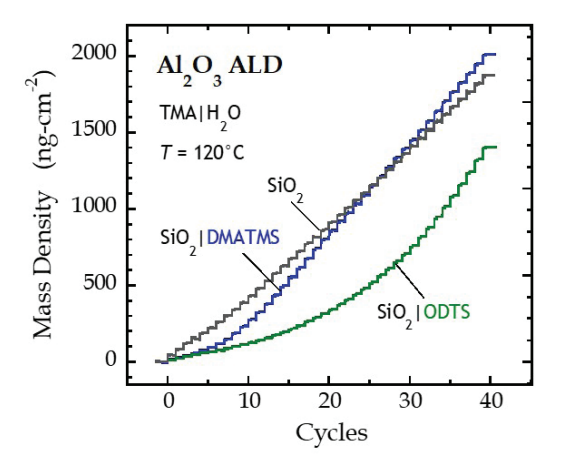


Figure 4: QCM data showing mass densities vs number of cycles for Al2O3 using TMA-Al \mid H2O process chemistry at T = 120 °C on SiO2 crystals passivated with either DMATMS or ODTS.

similar reaction conditions.

Conclusions and Future Steps:

We have shown that steric hindrance between the precursor and the blocking molecule plays an important role in blocking ALD growth on non-growth surfaces. Our future steps involve studying alternative precursors and blocking molecules to achieve ASD for a variety of thin films and surfaces.

- [1] Swarup, J. V; Chuang, H.-R.; You, A. L.; Engstrom, J. R. Effect of Co-Reactants on Interfacial Oxidation in Atomic Layer Deposition of Oxides on Metal Surfaces. ACS Appl Mater Interfaces 2024, 16 (13), 16983–16995. https://doi.org/10.1021/acsami.3c19033.
- [2] Swarup, J. V; Chuang, H.-R.; Jensen, J. T.; Gao, J.; You, A. L.; Engstrom, J. R. Nonpyrophoric Alternative to Trimethylaluminum for the Atomic Layer Deposition of Al2O3. Journal of Vacuum Science & Technology A 2025, 43 (2), 022404. https://doi.org/10.1116/6.0004171.

Mapping Structure Evolution During Lithiation of 2D Materials

CNF Project Number: 303522 Principal Investigator(s): Judy Cha Users(s): Natalie Williams, Sihun Lee

Affiliations(s): Department of Materials Science and Engineering, Cornell University; Department of Chemistry and Chemical Biology, Cornell University

Primary Source(s) of Research Funding: The Gordon and Betty Moore Foundation's EpiQS Initiative (GBMF9062.01); Department of Energy, Basic Energy Sciences program Grant No. DE-SC0023905

Contact: jc476@cornell.edu, nlw49@cornell.edu, sl2859@cornell.edu

Research Group Website: cha.mse.cornell.edu

Primary CNF Tools Used: Heidelberg DWL66FS, Heidelberg MLA 150 Maskless Aligner, SC4500 Odd-Hour & Even-Hour Evaporator

Abstract:

To study promising materials for lithium-ion batteries, it is essential to track complete phase evolutions throughout lithiation. Lithium intercalation, the process by which lithium ions are reversibly inserted into a host material, typically induces structural and electronic phase transitions in electrode materials [1], directly influencing battery capacity and cycling stability. Techniques such as in situ Raman spectroscopy, electrical transport, and x-ray diffraction provide valuable insights into structural transformations but lack the spatial resolution to visualize these changes at the nanoscale in real space. Among available experimental methods, scanning transmission electron microscopy (STEM) uniquely offers simultaneous imaging, diffraction, and spectroscopy at atomic-scale resolution. Here, we employ multimodal in situ 4D STEM, along with in situ Raman spectroscopy and electrochemical data using coin-type cells, to map nanoscale phase evolutions during lithium intercalation in the layered material LaTe₃.

Summary of Research:

Figure 1a illustrates the structure of LaTe₃, and Figure 1b depicts the geometry of our electrochemical cell, which varies slightly based on experimental requirements. In situ Raman spectroscopy identifies four distinct lithiation phases in LaTe₃ (Figure 2b). The initial phase corresponds to the pristine state of LaTe₃ at open-circuit voltage (OCV). At the first phase transition, phonon modes associated with the charge density wave (CDW) of LaTe₃ disappear and are replaced by new modes that evolve continuously throughout lithiation. Optical imaging reveals dark lines forming on the flakes during lithiation, which are wrinkles caused by strain relaxation from structure transformations (Figure 2a).

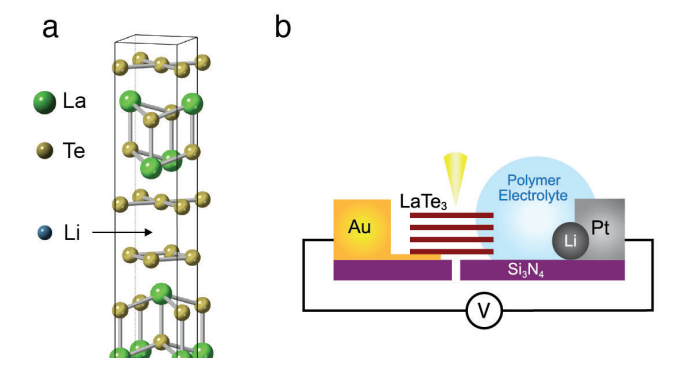
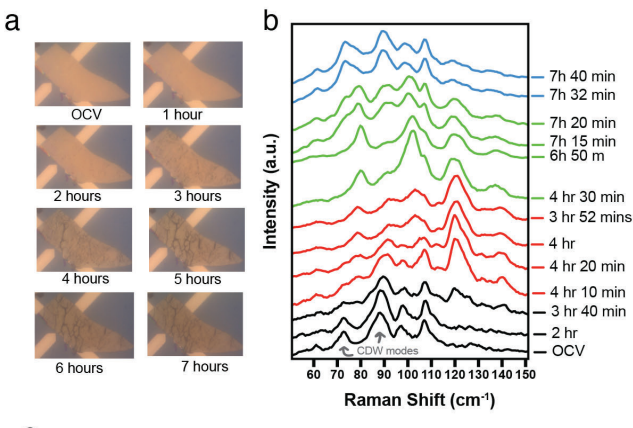


Figure 1: (a) Crystal structure of LaTe3. Li ions are intercalated electrochemically between the Te sheets. (b) Schematic of an electrochemical cell on a S/TEM e-chip for multimodal in situ STEM experiments.

A galvanostatic discharge curve from a LaTe3 coin-cell similarly portrays four distinct lithiation phases (Figure 2b).

To gain deeper insight into the lithiated phases, we performed an in situ lithiation experiment to acquire complementary datasets using STEM, including atomicresolution and low-magnification STEM imaging, electron energy loss spectroscopy (EELS), and spatially resolved four-dimensional diffraction (4D STEM) using an Electron Microscopy Pixel Array Detector (EMPAD) [2]. Figure 3a shows electron diffraction acquired during in situ 4D STEM lithiation of LaTe3. The original CDW is suppressed, as indicated by the disappearance of superlattice peaks at $q = 2/7c^*$ at the first phase transition, corroborating Raman results. A new lithiuminduced superlattice emerges at $q = 1/3c^*$, accompanied by changes in LaTe₃ layer stacking, seen in the varying intensities of lithium ordering peaks. We also observe initial in-plane lattice expansion followed by relaxation, along with evolving lithium occupancy in the host lattice. Ultimately, as lithium becomes fully incorporated, all ordering peaks vanish. Concurrent in



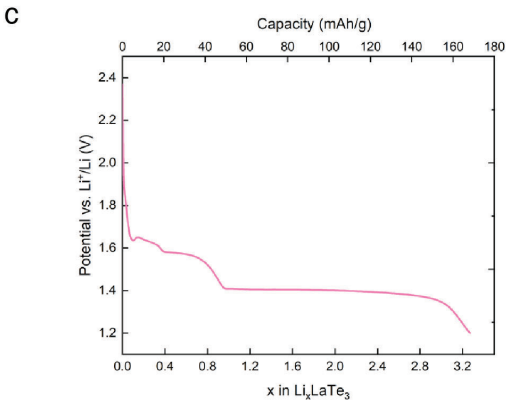


Figure 2: (a) Optical images and (b) in situ Raman spectra during lithiation of LaTe3. (c) Galvanostatic discharge curve of LaTe3 coin cell, suggesting three distinct lithated phases.

situ EELS confirms the emergence and gradual increase of lithium content during intercalation (Figure 3b).

Conclusions and Future Steps:

We have successfully mapped structural, chemical, and electronic transitions in LaTe₃ induced by lithium intercalation through combined in situ Raman spectroscopy, electrochemical data of coin-cells, and multimodal in situ STEM techniques (imaging, EELS, and 4D STEM). The observed lithiated phases of LaTe3 are new and have not been observed previously. Our methodology provides a robust framework applicable to future investigations of phase transformations in other intercalation materials.

- M. Wang, S. Xu, and J. J. Cha, "Revisiting Intercalation-Induced Phase Transitions in 2D Group VI Transition Metal Dichalcogenides," Advanced Energy and Sustainability Research, vol. 2, no. 8, p. 2100027, 2021, doi: 10.1002/ aesr.202100027.
- [2] M. W. Tate et al., "High Dynamic Range Pixel Array Detector for Scanning Transmission Electron Microscopy," Microscopy and Microanalysis, vol. 22, no. 1, pp. 237–249, Feb. 2016, doi: 10.1017/S1431927615015664.

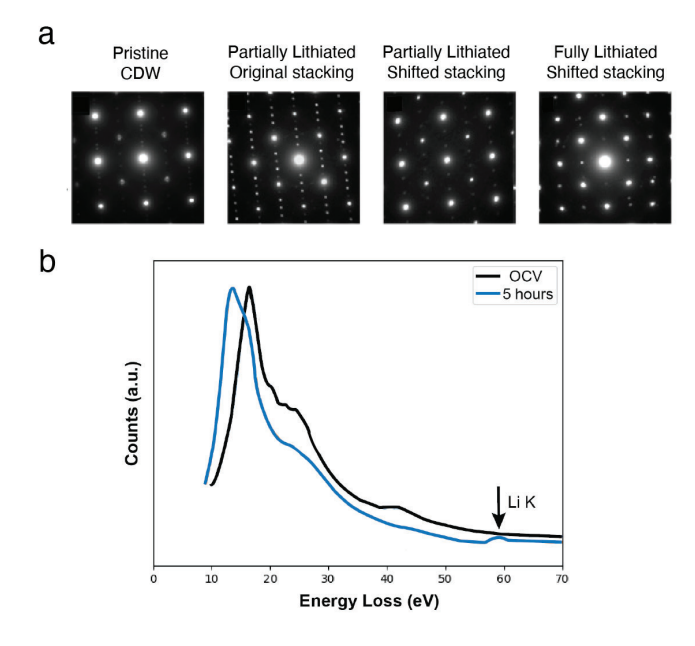


Figure 3: (a) Diffraction patterns of the four main structures acquired during in situ STEM of lithium intercalation into LaTe3. (b) Low loss EEL spectra from 2 points in the experiment, depicting the emerging Lithium K-edge edge in the host lattice.

Spore-Polymer Composite Materials

CNF Project Number: 308523

Principal Investigator(s): Meredith Silberstein

User(s): Ellen van Wijngaarden

Affiliation(s): Sibley School of Mechanical and Aerospace Engineering Primary Source(s) of Research Funding: Office of Naval Research Contact: silbersteinlab.com, mt845@cornell.edu, ewv8@cornell.edu

Research Group Website: silbersteinlab.com

Primary CNF Tools Used: Lyophilizer, PDMS Casting Station

Abstract:

Repeated loading on materials leads to fatigue cracking and eventually, catastrophic failure. Current methods for crack detection, such as visual inspection or ultrasonic testing are expensive, require equipment downtime and do not mitigate cracks that are detected. Living materials achieve novel functionalities through leveraging living organisms to sense and respond to changes in the environment, such as a crack. We designed a bacterialpolymer composite coating capable of detecting fatigue cracking and with the potential to regulate the crack conditions to mitigate cracking in the substrate. This study demonstrates crack detection for various substrate geometries and loading conditions. Ultimately, early crack detection will reduce material waste, increase product lifespan, and improve safety through preventing failure.

Summary of Research:

Fatigue cracking due to repeated loading, eventually leads to failure in all materials. Engineers are continuously looking to develop fatigue resistant materials and early crack detection methods to mitigate the safety risk.[1] Designing living materials presents a novel method of detecting cracks by leveraging living organisms' ability to sense and respond to the environment. Living materials combine conventional synthetic matrices with live organisms to expand the functionality of materials. Extensive progress has been made in developing bacteria-based materials that can self-heal and sense chemicals in the environment.[2,3] However, maintaining a viable living material remains a significant roadblock. Bacterial spores provide a robust option that enables bacteria cells to survive harsh conditions in a dormant, spore, state.[4] Bacterial spores are capable of surviving ultraviolet light exposure, drastic temperature shifts, and lack of nutrients. [5] We have integrated bacterial spores into a material system to produce a functional coating capable of detecting cracks via fluorescence. Our work explores the material coating design and material selection process. Lastly, we demonstrate the versatility of our coating for different geometries and loading conditions for in situ fatigue crack detection.

The tools and technical expertise provided at the CNF was essential to the rapid testing necessary for biological samples. Future work will investigate different polymer matrix options for obtaining varied material properties. We will also expand on our preliminary tests to include genetically modified spores to respond to specific germinants for sensing applications.

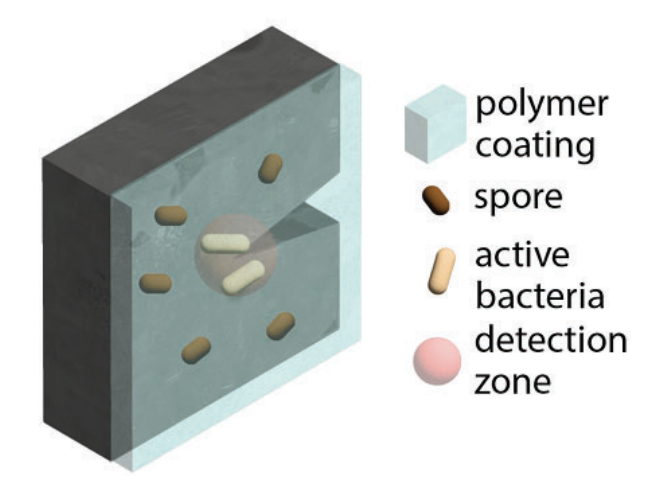


Figure 1: Bacteria-based fatigue crack detection and mitigation concept schematic.

- [1] P. Paris, M. Gomez, W. Anderson, Trends Engin. 1961, 13, 9.
- [2] H. Jonkers, Self Healing Concrete: A Biological Approach, Vol. 100, Springer, Dordrecht, 2007.
- [3] L. Gao, L. Feng, D. F. Sauer, M. Wittwer, Y. Hu, J. Schiffels, X. Li, Cell Rep. Phys. Sci. 2022, 3, 101054.
- [4] F. Lyu, T. Zhang, M. Gui, Y. Wang, L. Zhao, X. Wu, L. Rao, X. Liao, CRFSFS 2023, 22, 2728.
- [5] E. Black, P. Setlow, A. Hocking, C. Stewart, A. Kelly, D. Hoover, Compr. Rev. Food Sci. Food Saf. 2007, 6, 103.

Biphilic Porous Transport Layer Enabled High Efficiency and Highcurrent Density Proton Exchanger Membrane Electrolyzer

CNF Project Number: 322324

Principal Investigator(s): Lenan Zhang

User(s): Paranut Aksornsiri

Affiliation(s): Sibley School of Mechanical and Aerospace Engineering, Cornell University Primary Source(s) of Research Funding: Electricity Generating Authority of Thailand

Contact: Izhang@cornell.edu, pa379@cornell.edu

Research Group Website: https://sites.google.com/view/energy-research-lab/home Primary CNF Tools Used: ABM Contact Aligner, Heidelberg MLA 150 Maskless Aligner

Abstract:

Green hydrogen is considered one of the most promising energy carriers for achieving carbon neutrality, offering a scalable solution for long-duration, high-energy-density energy storage. Among various production technologies, proton exchange membrane water electrolysis (PEMWE) stands out due to its high energy efficiency, compatibility with intermittent renewable energy sources, and ability to generate high-purity hydrogen.

However, at high current densities, PEMWE systems suffer from significant mass transport losses, particularly due to limitations in water and gas transport within the porous transport layer (PTL). [1,2]

This research proposes a novel design for the PTL aimed at enabling ultrahigh current density operation (>5 A/cm²) with enhanced energy efficiency. The design introduces a biphilic pattern (figure 1), comprising spatially alternating hydrophilic and hydrophobic regions, into the PTL to facilitate mass transport. Hydrophilic regions promote continuous water delivery to the catalyst layer, while hydrophobic regions facilitate oxygen gas removal. The biphilic pattern is fabricated using photolithographic techniques, followed by coating of hydrophobic particles. After development and photoresist removal, the resulting PTL exhibits distinct wetting regions. Preliminary analysis suggests that this design may double the energy efficiency under ultrahigh current density conditions.

Summary of the Research:

The proposed biphilic pattern is designed to enhance mass transport on the anode side of the PEM electrolyzer by facilitating the removal of oxygen bubbles through dry hydrophobic channels. These hydrophobic regions leverage capillary pressure in the PTL's microstructure

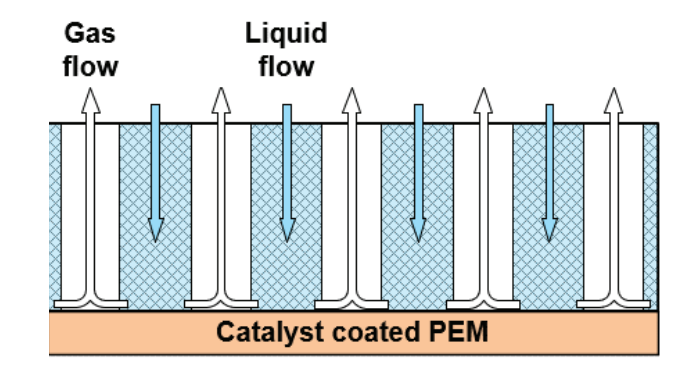


Figure 1: Figure 1: Schematic illustration of the biphilic porous transport layer (PTL) design.

to drive oxygen out of the cell, while hydrophilic regions ensure continuous water supply to the catalyst layer. This spatial separation of gas and liquid transport pathways minimizes bubble accumulation on the catalyst surface, therefore reducing overpotentials and enhancing overall electrochemical performance [3].

To demonstrate the feasibility of the patterning approach, initial experiments were conducted on silicon wafers due to their flat geometry and ease of processing. A thin layer of P20 MICROPOSITTM PRIMER was applied, followed by spin-coating of SHIPLEY MICROPOSITTM S1827 photoresist. After soft baking, the samples were exposed to UV light using an ABM contact aligner and developed to define the desired pattern. The developed samples were then uniformly coated with hydrophobic particles. Finally, the photoresist was removed using MICROPOSITTM REMOVER, leaving hydrophobic particles only on the exposed regions, thereby forming the intended biphilic pattern. As shown in Figure 2, water droplets deposited on each region exhibit distinctly different contact angles, confirming successful formation of a biphilic surface.

Subsequently, the fabrication was extended to titanium PTL substrates. The samples were diced to the desired size using a DISCO dicing saw. A simplified design—



Figure 2: Water droplets on silicon wafer demonstrating biphilic pattern formation.



Figure 3: Water droplets on titanium porous transport layer with a simplified biphilic pattern.

comprising one large hydrophilic region adjacent to a large hydrophobic region—was fabricated to examine wetting contrast by following the same procedure as the silicon wafers. Figure 3 displays the resulting patterned PTL.

However, experimental observations revealed incomplete removal of hydrophobic particles from the photoresist-covered areas, resulting in partial hydrophobicity in regions intended to be hydrophilic. The final photomask design, generated using the Heidelberg Mask Writer DWL2000, was successfully used to produce high-resolution micro-patterns on titanium substrates, though the final coating step is pending resolution of the contamination issue.

Conclusions and Future Plans:

Microscale patterning was successfully achieved on both silicon and porous titanium substrates. However, the incomplete removal of hydrophobic particles remains a key challenge, affecting the fidelity of the biphilic pattern. Future work will focus on enhancing the contrast between hydrophilic and hydrophobic regions through optimized cleaning procedures, including alkaline treatment and plasma exposure. Additionally, further refinement of the photolithography parameters will be pursued to improve resist coating uniformity on the porous PTL surface and ensure pattern integrity. These steps are critical to fully realizing the potential of the proposed PTL design for high-efficiency PEMWE operation.

- M. R. Domalanta et al., Pathways towards Achieving High Current Density Water Electrolysis: from Material Perspective to System Configuration, ChemSusChem, 16, e202300310, 2023.
- [2] J. K. Lee et al., Critical Current Density as a Performance Indicator for Gas-Evolving Electrochemical Devices, Cell Reports Physical Science, 1, 100147, 2020.
- [3] Y. Yang et al., Improving Mass Transfer with Surface Patterning of the Porous Transport Layer for PEM Water Electrolysis, Cell Reports Physical Science, 6, 102433, 2025.